

# Xenon isotopic constraints on the history of volatile recycling into the mantle

Rita Parai<sup>1\*</sup> & Sujoy Mukhopadhyay<sup>2</sup>

**The long-term exchange of volatile species (such as water, carbon, nitrogen and the noble gases) between deep Earth and surface reservoirs controls the habitability of the Earth's surface. The present-day volatile budget of the mantle reflects the integrated history of outgassing and retention of primordial volatiles delivered to the planet during accretion, volatile species generated by radiogenic ingrowth and volatiles transported into the mantle from surface reservoirs over time. Variations in the distribution of volatiles between deep Earth and surface reservoirs affect the viscosity, cooling rate and convective stress state of the solid Earth. Accordingly, constraints on the flux of surface volatiles transported into the deep Earth improve our understanding of mantle convection and plate tectonics. However, the history of surface volatile regassing into the mantle is not known. Here we use mantle xenon isotope systematics to constrain the age of initiation of volatile regassing into the deep Earth. Given evidence of prolonged evolution of the xenon isotopic composition of the atmosphere<sup>1,2</sup>, we find that substantial recycling of atmospheric xenon into the deep Earth could not have occurred before 2.5 billion years ago. Xenon concentrations in downwellings remained low relative to ambient convecting mantle concentrations throughout the Archaean era, and the mantle shifted from a net degassing to a net regassing regime after 2.5 billion years ago. Because xenon is carried into the Earth's interior in hydrous mineral phases<sup>3–5</sup>, our results indicate that downwellings were drier in the Archaean era relative to the present. Progressive drying of the Archaean mantle would allow slower convection and decreased heat transport out of the mantle, suggesting non-monotonic thermal evolution of the Earth's interior.**

Volatiles are degassed from the interior to Earth's surface reservoirs during partial melting of upwelling mantle. Conversely, downwelling mantle transports material from Earth's surface to the deep interior. Some volatiles are removed from downwellings and expelled back to the surface via magmatism, but some may be retained within downwellings and ultimately mixed into the convecting mantle (that is, the mantle source of mid-ocean ridge basalts). Here we use the term 'regassing' to indicate the transport of surface volatiles into the mantle beyond depths of magma generation and subsequent mixing into the convecting mantle. In early Earth history, downwelling return flow may have differed in nature from modern subduction<sup>6</sup>, where surface volatiles are regassed into the mantle in association with hydrothermally altered subducting slabs<sup>7–10</sup>. The nature of early downwellings and the timing of the onset of substantial volatile regassing are not known.

Xe isotopes provide a powerful tool with which to probe the history of volatile cycling on the Earth. The nine isotopes of Xe provide insight into the integrated history of mantle volatile delivery, degassing and regassing: <sup>124</sup>Xe, <sup>126</sup>Xe, <sup>128</sup>Xe and <sup>130</sup>Xe are primordial, radiogenic <sup>129</sup>Xe is produced by decay of short-lived <sup>129</sup>I, and <sup>131</sup>Xe, <sup>132</sup>Xe, <sup>134</sup>Xe and <sup>136</sup>Xe are produced in characteristic proportions and on different timescales by the spontaneous fission of short-lived <sup>244</sup>Pu (half-life of  $t_{1/2} = 80.0$  Myr) and long-lived <sup>238</sup>U ( $t_{1/2} = 4.468$  Gyr). Degassing fractionates lithophile parent isotopes from atmosphere Xe daughter

isotopes, so that mantle Xe isotopic compositions are sensitive to degassing on a variety of timescales. Critically, mantle Xe is also sensitive to volatile regassing: atmospheric Xe, which is isotopically distinct from mantle Xe, has been regassed to the deep Earth in sufficient quantities to affect mantle Xe isotopic compositions<sup>11–16</sup>.

The isotopic composition of atmospheric Xe available for regassing has varied over time. Compared to primordial noble gas compositions, the Earth's modern atmosphere is depleted in Xe relative to other noble gases, and atmospheric Xe is isotopically mass-fractionated<sup>17–19</sup>. These observations are attributed to mass-fractionating loss of Xe from the atmosphere. Xe measured in fluid inclusions in Archaean rocks of different age indicate that this process was protracted and that the modern atmospheric composition was attained about 2.0 Gyr ago<sup>1,2</sup> (Extended Data Fig. 1). If atmospheric volatiles were regassed into the deep Earth throughout Earth history, then the mantle has received a mixture of modern and ancient atmospheric Xe isotopic compositions over time.

Assuming that all regassed atmospheric Xe is modern, the present-day mantle Xe budget is found to be dominated by regassed atmospheric Xe<sup>12,14–16</sup> (~80%–90%, consistent with estimates of the proportion of regassed atmospheric Xe from the stable, non-radiogenic isotopes of Xe in continental well gases<sup>11</sup>). If all regassed Xe instead had the isotopic composition estimated for the atmosphere 3.3 Gyr ago<sup>20</sup>, then the present-day upper-mantle Xe composition could not be explained (Extended Data Fig. 2). This test of end-member scenarios suggests that the budget of regassed atmospheric Xe retained within the mantle today is likely to be predominantly modern (<2.0 Gyr ago<sup>2</sup>) in its isotopic composition, consistent with two possible scenarios: (a) early Xe regassing was suppressed, perhaps as high mantle potential temperatures promoted shallow release of atmospheric volatiles from downwelling material in the past, or (b) substantial quantities of ancient (>2.0 Gyr ago) atmospheric Xe were regassed beyond depths of magma generation into the deep Earth, but strong subsequent mantle degassing, in association with high mantle processing rates, depleted the mantle of ancient regassed volatiles. High mantle processing rates would promote both strong degassing and concurrent regassing if Xe were retained in downwellings early in Earth history. Intensive degassing and regassing would diminish the mantle radiogenic (<sup>129</sup>Xe) and fissionogenic (<sup>131,132,134,136</sup>Xe) excesses relative to the atmosphere and would affect the proportion of <sup>244</sup>Pu-derived to <sup>238</sup>U-derived fissionogenic xenon. To distinguish between scenarios (a) and (b), it is thus necessary to explicitly model continuous degassing, regassing and fissionogenic production in the mantle over time.

We use a forward model of mantle Xe transport and ingrowth to explore limits on the history of Xe regassing into the mantle. We apply three model forcings (Fig. 1). (1) We prescribe a mass-fractionating atmospheric Xe isotopic composition over time on the basis of data from Archaean rocks<sup>2</sup> (Extended Data Fig. 1). (2) The mantle processing-rate history is explored as a free parameter. (3) The concentration of Xe retained in downwellings beyond depths of magma generation over time (<sup>130</sup>Xe<sub>d</sub> time series, referred to here as 'regassing history') is

<sup>1</sup>Department of Earth and Planetary Sciences, Washington University in St. Louis, Saint Louis, MO, USA. <sup>2</sup>Department of Earth and Planetary Sciences, University of California, Davis, Davis, CA, USA. \*e-mail: parai@wustl.edu

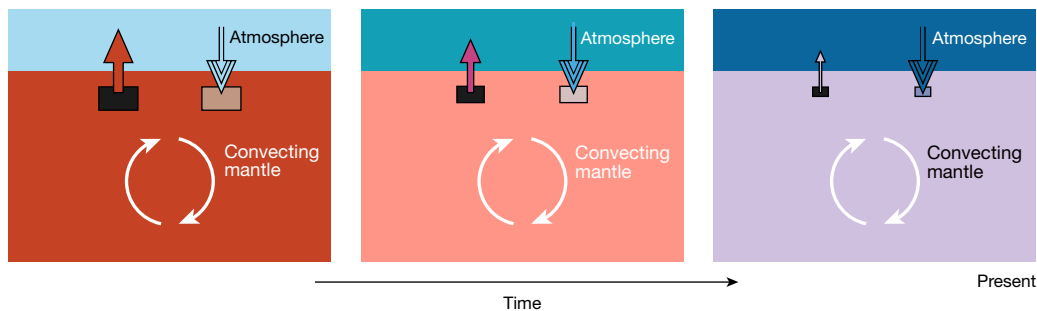


**Fig. 1 | Conceptual model of mantle degassing, regassing and fissionogenic production.** At a given time step, a parcel of upwelling mantle undergoes partial melting and is completely degassed of its Xe contents (red, pink and purple arrows). An equal mass of downwelling material carries atmospheric Xe to be regassed into the mantle (blue arrows). Convective mixing is indicated by the white arrows. The mantle processing rate decreases over time (as illustrated by the smaller processed-mantle boxes). Many different potential regassing histories ( $^{130}\text{Xe}_d$ ) are tested over time (indicated by the multiple blue arrows). Atmospheric Xe undergoes mass-dependent fractionation over time until 2 Gyr ago (as illustrated by the different shades of blue in the atmosphere box). The net change in  $^{130}\text{Xe}$  in the mass of mantle that is processed at a given time step is the

explored as a free parameter set. (A summary of the notation used in the paper is given in Extended Data Table 1.) The initial mantle  $^{130}\text{Xe}$  concentration is taken to be consistent with a late-veneer contribution of Xe from carbonaceous chondrites of 0.1%–1% of the Earth's mass<sup>21</sup>, although we note that the primordial Xe budget may have been partially acquired during the main stage of accretion. The initial mantle Xe isotopic composition is taken to be that of average carbonaceous chondrite<sup>17,18,22</sup>. The Xe isotopic composition of the atmosphere is modelled by a Rayleigh fractionation trajectory towards the modern composition (Extended Data Fig. 1). We search for Xe regassing histories that yield mantle compositions consistent with Xe isotopic and concentration constraints from the literature (Methods, Extended Data Table 2).

The mantle processing-rate history describes the changing mass flux (in grams per unit time) of upwelling mantle that undergoes partial melting at the surface over time. We assume that partial melting results in complete degassing of the processed mantle mass. The degassing Xe flux at any given time is thus determined by the instantaneous processing rate and Xe concentration in the mantle. An equal mass flux of downwelling mantle carries regassed surface Xe into the deep mantle (Fig. 1). The regassing Xe flux at any given time thus reflects the instantaneous processing rate and Xe concentration in downwellings,  $^{130}\text{Xe}_d$ . We use an exponentially decreasing mantle processing rate pinned at the present-day mid-ocean ridge processing rate. Different processing-rate histories are explored through variation in the exponential time constant ( $\eta$ ; see Methods). The mantle processing-rate history may be expressed in terms of the number of mantle reservoir masses processed over Earth history ( $N_{\text{res}}$ ). We use values of  $\eta$  that yield whole number values of  $N_{\text{res}}$  and explore the effect of varying the size of the convecting mantle relative to the whole mantle ( $M_{\text{res}} = 50\%–90\%$ ).

To track fissionogenic Xe ingrowth concurrently with degassing and regassing, U and Pu concentrations must be tracked in the mantle over time. The initial mantle U concentration is taken to be 21 parts per billion (p.p.b.; bulk silicate Earth), and the initial  $^{244}\text{Pu}$  concentration is computed assuming an initial  $^{244}\text{Pu}/^{238}\text{U}$  ratio based on chondrites (Methods). U and Pu are partially sequestered into the continental crust over time. Both species are highly incompatible; however, the extraction of U and Pu from the mantle during partial melting may be offset by recycling of U- and Pu-rich materials in downwellings at a given time step. To model net extraction, U and Pu loss from the mantle at each time step directly tracks continental crustal growth over time (Extended Data Fig. 3, Methods).

The amount of atmospheric Xe recycled beyond depths of magma generation into the Earth's interior varied over time, as downwelling

difference between the instantaneous mantle  $^{130}\text{Xe}$  concentration and the instantaneous  $^{130}\text{Xe}_d$ . Assuming instantaneous mixing, the net change is distributed from the processed mantle parcel to the full convecting mantle reservoir. Concentrations of all other Xe isotopes in the mantle are computed using the instantaneous mantle isotopic composition for degassing, the instantaneous atmospheric Xe isotopic composition for regassing, and the instantaneous mantle  $^{238}\text{U}$  and  $^{244}\text{Pu}$  concentrations to determine fissionogenic ingrowth of  $^{131,132,134,136}\text{Xe}$  (Methods). The convecting mantle  $^{130}\text{Xe}$  concentration and Xe isotopic composition accordingly evolve over time in response to mantle degassing, regassing of atmospheric Xe with a changing isotopic composition and Xe production by spontaneous fission.

lithologies and mantle pressure–temperature conditions evolved on a cooling Earth. We use our model to test many different regassing histories ( $^{130}\text{Xe}_d$ ; Fig. 2). A Monte Carlo numerical approach is used to achieve efficient coverage of a wide regassing history parameter space: for each model realization, a different potential regassing history is

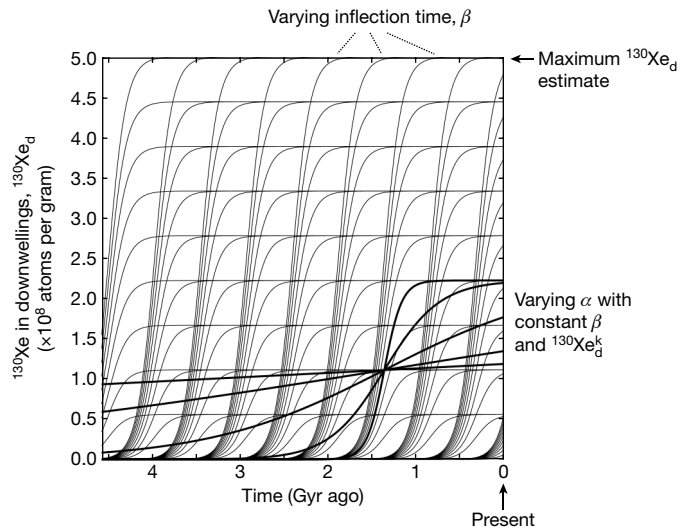


**Fig. 2 | Example sigmoidal regassing histories.** Three numerical parameters describe the sigmoid (Methods):  $^{130}\text{Xe}_d^k$  is the downwelling  $^{130}\text{Xe}$ -carrying capacity,  $\alpha$  is the growth rate and  $\beta$  is the sigmoid inflection time. A Monte Carlo numerical method is used to explore the parameter space efficiently and test a wide variety of sigmoidal  $^{130}\text{Xe}_d$  time series. Light-grey lines represent a collection of sigmoids with constant  $\alpha$  and 10 different  $^{130}\text{Xe}_d^k$  and  $\beta$  values. Thick solid black lines illustrate the result of varying the growth rate,  $\alpha$ , for a single ( $^{130}\text{Xe}_d^k$ ,  $\beta$ ) pair. Sampling a limited time interval yields only a portion of the sigmoid shape, such that the initial  $^{130}\text{Xe}_d$  values may be greater than 0, and the present-day  $^{130}\text{Xe}_d$  values are lower than or equal to the carrying capacity,  $^{130}\text{Xe}_d^k$ . The growth rate is allowed to vary between  $10^{-10}$  Gyr $^{-1}$  and  $10^{-8}$  Gyr $^{-1}$ , with small  $\alpha$  corresponding to slow growth. The inflection time is allowed to vary between 0.08 Gyr and 10 Gyr after the formation of the Solar System, and the carrying capacity ranges from 0 to an upper bound of  $5 \times 10^8$  atoms  $^{130}\text{Xe}$  per gram (Methods). Extended Data Fig. 3 shows examples of exponential  $^{130}\text{Xe}_d$  time series for comparison. A sigmoidal functional form enables testing of a wide variety of regassing histories, including near-linear, near-exponential and step functions.

determined by randomly drawing values for the parameters that define  $^{130}\text{Xe}_d$  as a function of time (Methods, Extended Data Table 1). A diverse assortment of regassing histories are tested using a sigmoidal  $^{130}\text{Xe}_d$  functional form (Fig. 2; see Extended Data Fig. 3 for exponential  $^{130}\text{Xe}_d$  examples).

Over a given time step, the net change in mantle  $^{130}\text{Xe}$  concentration represents the balance between  $^{130}\text{Xe}$  lost by degassing of the mantle mass processed by partial melting and  $^{130}\text{Xe}$  gained by regassing via a corresponding downwelling mass with concentration  $^{130}\text{Xe}_d$  (Fig. 1). Regassing of  $^{130}\text{Xe}$  is computed on the basis of  $^{130}\text{Xe}_d$  and the instantaneous atmospheric  $^{128,131,132,134,136}\text{Xe}/^{130}\text{Xe}$  composition. Fissionogenic production is calculated using the instantaneous concentrations of  $^{238}\text{U}$  and  $^{244}\text{Pu}$  in the convecting mantle (Methods). The model thus tracks how the  $^{130}\text{Xe}$  concentration and Xe isotopic composition in the mantle ( $^{128}\text{Xe}/^{130}\text{Xe}$ ,  $^{128}\text{Xe}/^{132}\text{Xe}$ ,  $^{130}\text{Xe}/^{132}\text{Xe}$ ,  $^{131}\text{Xe}/^{132}\text{Xe}$ ,  $^{134}\text{Xe}/^{132}\text{Xe}$  and  $^{136}\text{Xe}/^{132}\text{Xe}$ ) respond to degassing, regassing and fissionogenic production. Xe isotopic evolution paths corresponding to four potential regassing histories illustrate how the mantle Xe isotopic composition changes over time in response to model forcings (Fig. 3). A model realization is successful if two criteria are met: (1) the present-day concentration of  $^{130}\text{Xe}$  in the mantle falls within the estimated range of  $4.3 \times 10^5$  to  $9.2 \times 10^5$  atoms of  $^{130}\text{Xe}$  per gram (Methods) and (2) the present-day mantle Xe isotopic composition falls within the estimated convecting mantle composition field<sup>11,14,16,23</sup> (Fig. 3c, d, Extended Data Table 2).

Successful model realizations indicate that the concentration of regassed Xe retained in downwellings must have remained low (much lower than the mantle Xe concentration) until after about 2.5 Gyr ago (Fig. 4). Solutions correspond to a limited set of regassing histories, bounded by curves similar to C and D in Fig. 3: a near-zero  $^{130}\text{Xe}_d$  that increases rapidly to a modest final  $^{130}\text{Xe}_d$  in the last several hundred million years, and near-zero  $^{130}\text{Xe}_d$  that increases to a sustained low magnitude over the past  $\sim 2$  Gyr (Fig. 4a). On the basis of this analysis, the mantle shifted from net degassing to net regassing after about 2.5 Gyr ago (Fig. 4b, c). Accordingly,  $^{130}\text{Xe}_d$  concentrations were low relative to the convecting mantle  $^{130}\text{Xe}$  concentration until the Proterozoic at the earliest. Sustained low-magnitude  $^{130}\text{Xe}_d$  (curve D in Fig. 3, light-blue curves in Fig. 4) yields an earlier shift to net regassing, whereas regassing histories with a late increase in  $^{130}\text{Xe}_d$  yield a late shift to regassing and rapid recent change in mantle Xe isotopic composition (curve C in Fig. 3, dark-blue lines in Fig. 4, Extended Data Fig. 4). Constraints on Xe isotopic compositions in mantle-derived rocks over time would distinguish between viable regassing histories. We note that the results are robust among solutions derived using different initial mantle  $^{130}\text{Xe}$  concentrations, mantle processing parameters and  $^{130}\text{Xe}_d$  functional forms (Extended Data Figs. 5–7). In all successful model realizations, we find that the dominance of the modern atmospheric Xe isotopic signature in present-day mantle sources requires limited early regassing of ancient atmospheric Xe into the mantle (scenario (a) above).

Previous studies have shown that hydrous minerals in subducting lithologies carry Xe<sup>5,24,25</sup> and that the abundance pattern of heavy noble gases in the mantle reflects incorporation of noble gases associated with hydrous minerals into the mantle<sup>5,26,27</sup>. Because hydrous minerals carry Xe, H<sub>2</sub>O cannot be regassed into the mantle without also regassing some Xe into the mantle. Limited early regassing of Xe therefore provides a constraint on early regassing of H<sub>2</sub>O. The ratio of chemically bound H<sub>2</sub>O to Xe varies among serpentinites, altered oceanic crust and sediments. If we take the distribution of  $^{130}\text{Xe}_d$  values at 3 Gyr ago from successful model realizations and estimate the H<sub>2</sub>O/ $^{130}\text{Xe}$  ratio of serpentinite (a high H<sub>2</sub>O/Xe lithology) as  $1.2 \times 10^{13}$  (13 wt% H<sub>2</sub>O and  $3.7 \times 10^8$  atoms  $^{130}\text{Xe}$  per gram<sup>5</sup>), then the median H<sub>2</sub>O concentration in downwellings at 3 Gyr ago is  $\sim 0.61$  p.p.m. H<sub>2</sub>O and 95% of solutions have between  $\sim 0$  and 62 p.p.m. H<sub>2</sub>O. This range suggests very dry conditions compared to the estimated  $\sim 400$ – $1,000$  p.p.m. H<sub>2</sub>O concentration in present-day slabs subducting beyond depths of magma generation<sup>9,10,28</sup>. If some Xe were regassed via materials with relatively

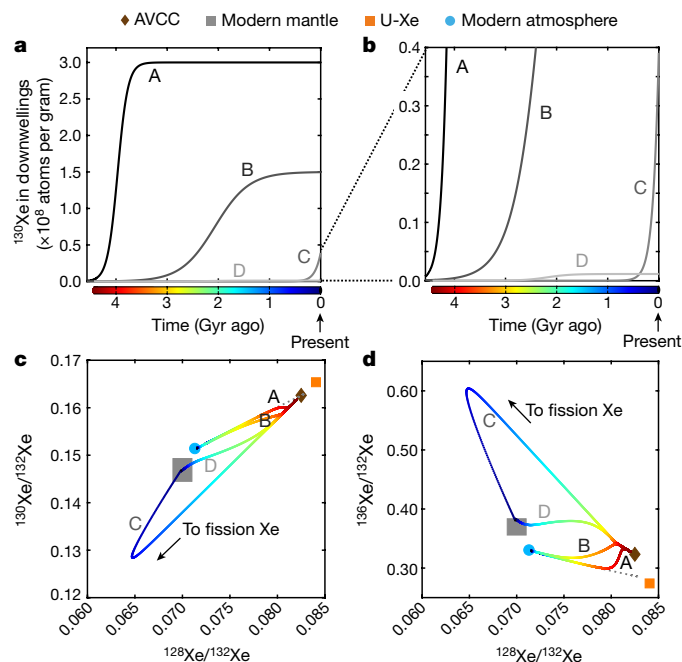
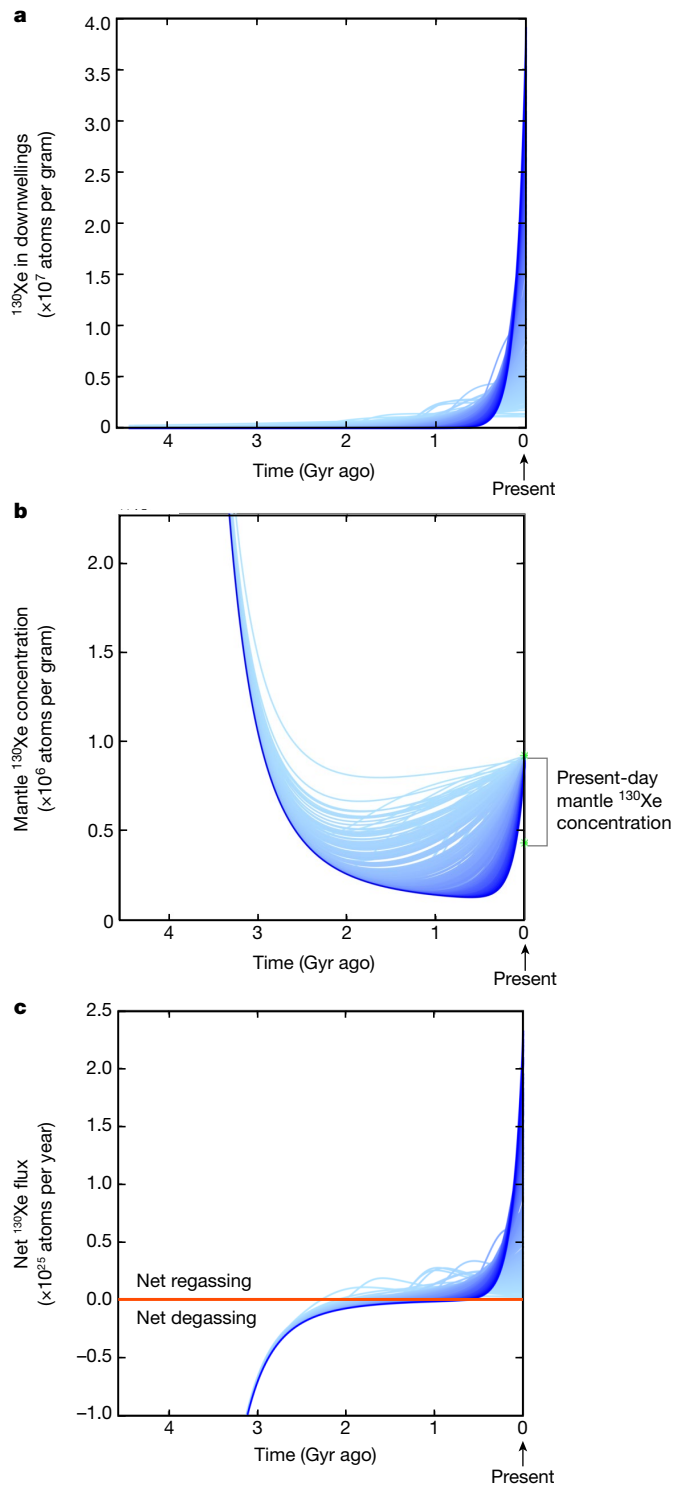


**Fig. 3 | Mantle isotopic evolution curves.** **a, b**, Four different regassing histories (A, B, C and D) are tested assuming an initial mantle  $^{130}\text{Xe}$  concentration of  $3.2 \times 10^8$  atoms per gram, a convecting mantle reservoir that is 90% of the mass of the whole mantle and 8 mantle-reservoir masses processed over Earth history. **c, d**, The corresponding mantle isotopic evolution curves (rainbow-coloured according to time) show how the mantle  $^{128,130,132,136}\text{Xe}$  composition responds to degassing, regassing and fissionogenic production over time. The initial mantle composition is average carbonaceous chondrite (AVCC, brown diamond). The present-day mantle field is represented by a dark-grey box (Extended Data Table 2). Successful regassing histories yield a present-day mantle Xe isotopic composition and  $^{130}\text{Xe}$  concentration within the field constrained by mantle Xe data. The atmosphere starts with a composition that is mass-fractionated by 39‰ per atomic mass unit relative to the modern atmosphere (similar to U-Xe<sup>17–19</sup>, which is an estimate of the primordial atmospheric composition; orange square) and follows a Rayleigh mass-fractionation trend (dashed grey curve) to reach the modern atmospheric composition (light-blue circle) at 2.5 Gyr ago (Extended Data Fig. 1). Degassing drives mantle Xe isotope ratios towards Pu-fission and U-fission Xe compositions defined in Extended Data Table 2. Regassing drives mantle Xe isotope ratios towards the instantaneous atmospheric Xe composition. Strong regassing (curves A, B) puts too much atmospheric Xe in the mantle, so that the Xe isotopic composition of the mantle largely reflects the evolving atmospheric composition, despite fissionogenic production. The present-day mantle composition is achieved with regassing histories that have limited regassing until  $\sim 2.5$  Gyr ago: either with negligible regassing through most of Earth history, increasing to modest regassing in the past few hundred million years (curve C), or with near-constant low-magnitude regassing over the past few billion years (curve D). Curves C and D represent the extremes of the successful regassing histories illustrated in Fig. 4a.

low H<sub>2</sub>O/Xe, such as sediments, then the amount of water in Archaean downwellings would have been even lower. We note that as pressure and temperature increases, diffusion and advection of fluids released by hydrous mineral breakdown may alter H<sub>2</sub>O/Xe ratios in downwellings. If advection via hydrous-breakdown fluids removes Xe, then H<sub>2</sub>O and Xe may remain coupled through subduction. Previous work indicates that dehydration of hydrous minerals may actually lower H<sub>2</sub>O/Xe ratios: dry olivine–enstatite residues formed by antigorite breakdown preserve Xe concentrations hundreds of times higher than that of the ambient upper mantle<sup>27</sup>. If Xe is primarily carried in fluid inclusions, diffusion may explain this observation: H<sup>+</sup> is expected to diffuse out of inclusions more readily than Xe, potentially leading to preferential loss of H<sub>2</sub>O relative to Xe at high pressures and temperatures<sup>5,27</sup>. Low H<sub>2</sub>O/Xe ratios after the breakdown of hydrous minerals or dessication



of fluid inclusions would further limit the concentration of  $\text{H}_2\text{O}$  that could have been regassed with Xe early in Earth history. Therefore, we suggest that on the basis of Xe isotopic constraints, downwellings before 2.5 Gyr ago were dry compared to modern-day subducting slabs.

We note that there is evidence for the initiation of subduction before the Proterozoic: eclogitic inclusions appear in diamonds 3.0 Gyr old and younger<sup>29</sup>, and Hadean zircon thermobarometry suggests that magma production in convergent margin-like environments occurred as early as 4.2 Gyr ago<sup>30</sup>. If plate tectonics and plate subduction were initiated before 2.5 Gyr ago, then early subducted material was either hydrated to a lesser extent at the surface than today, or volatiles were more efficiently expelled from Archaean slabs at shallow depths and returned to the surface. If high-temperature alteration of relatively

**Fig. 4 | Xe regassing is limited early in Earth history.** a–c, Time series showing regassing histories,  $^{130}\text{Xe}_d$ , for successful model realizations (a), the corresponding mantle  $^{130}\text{Xe}$  concentrations over time (b) and the net flux between the convecting mantle and atmosphere over time (c). Successful model realizations indicate minimal  $^{130}\text{Xe}$  in downwelling material until  $\sim 2.5$  Gyr ago. Line colour in all panels reflects the present-day  $^{130}\text{Xe}_d$  concentrations from a: darker blue indicates higher present-day  $^{130}\text{Xe}_d$  concentrations. Successful realizations with relatively high present-day  $^{130}\text{Xe}_d$  concentrations are associated with regassing onset times in the past few hundred million years (dark blue), whereas regassing histories with earlier onset times (1–2 Gyr ago) have very low present-day  $^{130}\text{Xe}_d$  concentrations (light blue; see Extended Data Fig. 4). Successful model realizations indicate that the mantle shifted from a net degassing regime to a net regassing regime about 2.5 Gyr ago or later:  $^{130}\text{Xe}_d$  concentrations were low relative to the convecting mantle  $^{130}\text{Xe}$  concentration until the Proterozoic at the earliest (b, c; Extended Data Fig. 8). The successful model regassing histories with the lowest and highest present-day  $^{130}\text{Xe}_d$  values (lightest and darkest blue curves, respectively) correspond to curves C and D in Fig. 3. Model results reflect an initial mantle  $^{130}\text{Xe}$  concentration of  $3.2 \times 10^8$  atoms per gram, a convecting mantle reservoir that is 90% of the mass of the whole mantle, 8 mantle-reservoir masses processed over Earth history and the continental crust growth model 1 (see Methods). Other parameter combinations and Xe fluxes are illustrated in Extended Data Figs. 5–7 and emphasize that regassing must have been limited early in Earth history.

thick Archaean crust in a Xe-rich early atmosphere promoted high initial  $^{130}\text{Xe}$  concentrations in surface-altered materials, then the latter effect must have dominated in order to yield low  $^{130}\text{Xe}_d$  concentrations. Independent of these physical factors, our results indicate that the convecting mantle experienced net degassing during the Archaean and transitioned to a net regassing regime after 2.5 Gyr ago.

### Online content

Any Methods, including any statements of data availability and Nature Research reporting summaries, along with any additional references and Source Data files, are available in the online version of the paper at <https://doi.org/10.1038/s41586-018-0388-4>

Received: 23 August 2017; Accepted: 5 June 2018;

Published online 8 August 2018.

- Pujol, M., Marty, B. & Burgess, R. Chondritic-like xenon trapped in Archaean rocks: a possible signature of the ancient atmosphere. *Earth Planet. Sci. Lett.* **308**, 298–306 (2011).
- Avice, G., Marty, B. & Burgess, R. The origin and degassing history of the Earth's atmosphere revealed by Archaean xenon. *Nat. Commun.* **8**, 15455 (2017).
- Ozima, M. & Podosek, F. A. *Noble Gas Geochemistry* (Cambridge University Press, Cambridge, 2002).
- Jackson, C. R., Parman, S. W., Kelley, S. P. & Cooper, R. F. Noble gas transport into the mantle facilitated by high solubility in amphibole. *Nat. Geosci.* **6**, 562–565 (2013).
- Kendrick, M. A. et al. Subduction zone fluxes of halogens and noble gases in seafloor and forearc serpentinites. *Earth Planet. Sci. Lett.* **365**, 86–96 (2013).
- Brown, M. Duality of thermal regimes is the distinctive characteristic of plate tectonics since the Neoproterozoic. *Geology* **34**, 961–964 (2006).
- Schmidt, M. W. & Poli, S. Experimentally based water budgets for dehydrating slabs and consequences for arc magma generation. *Earth Planet. Sci. Lett.* **163**, 361–379 (1998).
- Hacker, B. R.  $\text{H}_2\text{O}$  subduction beyond arcs. *Geochem. Geophys. Geosyst.* **9**, Q03001 (2008).
- van Keken, P. E., Hacker, B. R., Syracuse, E. M. & Abers, G. A. Subduction factory: 4. Depth-dependent flux of  $\text{H}_2\text{O}$  from subducting slabs worldwide. *J. Geophys. Res.* **116**, B01401 (2011).
- Parai, R. & Mukhopadhyay, S. How large is the subducted water flux? New constraints on mantle regassing rates. *Earth Planet. Sci. Lett.* **317–318**, 396–406 (2012).
- Holland, G. & Ballentine, C. J. Seawater subduction controls the heavy noble gas composition of the mantle. *Nature* **441**, 186–191 (2006).
- Mukhopadhyay, S. Early differentiation and volatile accretion recorded in deep-mantle neon and xenon. *Nature* **486**, 101–104 (2012).
- Parai, R., Mukhopadhyay, S. & Standish, J. J. Heterogeneous upper mantle Ne, Ar and Xe isotopic compositions and a possible Dupal noble gas signature recorded in basalts from the Southwest Indian Ridge. *Earth Planet. Sci. Lett.* **359–360**, 227–239 (2012).

14. Tucker, J. M., Mukhopadhyay, S. & Schilling, J. G. The heavy noble gas composition of the depleted MORB mantle (DMM) and its implications for the preservation of heterogeneities in the mantle. *Earth Planet. Sci. Lett.* **355–356**, 244–254 (2012).
15. Pető, M. K., Mukhopadhyay, S. & Kelley, K. A. Heterogeneities from the first 100 million years recorded in deep mantle noble gases from the Northern Lau Back-arc Basin. *Earth Planet. Sci. Lett.* **369–370**, 13–23 (2013).
16. Parai, R. & Mukhopadhyay, S. The evolution of MORB and plume mantle volatile budgets: constraints from fission Xe isotopes in Southwest Indian Ridge basalts. *Geochem. Geophys. Geosyst.* **16**, 719–735 (2015).
17. Pepin, R. O. On the origin and early evolution of terrestrial planet atmospheres and meteoritic volatiles. *Icarus* **92**, 2–79 (1991).
18. Pepin, R. O. On the isotopic composition of primordial xenon in terrestrial planet atmospheres. *Space Sci. Rev.* **92**, 371–395 (2000).
19. Pepin, R. O. & Porcelli, D. Origin of noble gases in the terrestrial planets. *Rev. Mineral. Geochem.* **47**, 191–246 (2002).
20. Pujol, M., Marty, B., Burnard, P. & Philippot, P. Xenon in Archean barite: weak decay of  $^{130}\text{Ba}$ , mass-dependent isotopic fractionation and implication for barite formation. *Geochim. Cosmochim. Acta* **73**, 6834–6846 (2009).
21. Marty, B. The origins and concentrations of water, carbon, nitrogen and noble gases on Earth. *Earth Planet. Sci. Lett.* **313–314**, 56–66 (2012).
22. Caracausi, A., Avice, G., Burnard, P. G., Füre, E. & Marty, B. Chondritic xenon in the Earth's mantle. *Nature* **533**, 82–85 (2016).
23. Caffee, M. et al. Primordial noble gases from Earth's mantle: identification of a primitive volatile component. *Science* **285**, 2115–2118 (1999).
24. Chavrit, D. et al. The contribution of hydrothermally altered ocean crust to the mantle halogen and noble gas cycles. *Geochim. Cosmochim. Acta* **183**, 106–124 (2016).
25. Matsuda, J. I. & Nagao, K. Noble gas abundances in a deep-sea sediment core from eastern equatorial Pacific. *Geochem. J.* **20**, 71–80 (1986).
26. Sumino, H. et al. Seawater-derived noble gases and halogens preserved in exhumed mantle wedge peridotite. *Earth Planet. Sci. Lett.* **294**, 163–172 (2010).
27. Kendrick, M. A., Scambelluri, M., Honda, M. & Phillips, D. High abundances of noble gas and chlorine delivered to the mantle by serpentinite subduction. *Nat. Geosci.* **4**, 807–812 (2011).
28. Korenaga, J., Planavsky, N. J. & Evans, D. A. Global water cycle and the coevolution of the Earth's interior and surface environment. *Phil. Trans. R. Soc. A* **375**, 20150393 (2017).
29. Shirey, S. B. & Richardson, S. H. Start of the Wilson cycle at 3 Ga shown by diamonds from subcontinental mantle. *Science* **333**, 434–436 (2011).
30. Hopkins, M., Harrison, T. M. & Manning, C. E. Low heat flow inferred from >4 Gyr zircons suggests Hadean plate boundary interactions. *Nature* **456**, 493–496 (2008).

**Acknowledgements** The project was funded by NSF grant EAR-1250419 to S.M. We thank D. Fike, C. Jackson, M. Krawczynski and S. Turner for discussions that improved the manuscript.

**Reviewer information** *Nature* thanks M. Kendrick and D. Porcelli for their contribution to the peer review of this work.

**Author contributions** S.M. and R.P. developed the conceptual model and the ideas presented in the manuscript. R.P. wrote the Matlab scripts for the numerical modelling. R.P. and S.M. analysed the results and R.P. wrote the manuscript with input from S.M.

**Competing interests** The authors declare no competing interests.

#### Additional information

**Extended data** is available for this paper at <https://doi.org/10.1038/s41586-018-0388-4>.

**Reprints and permissions information** is available at <http://www.nature.com/reprints>.

**Correspondence and requests for materials** should be addressed to R.P.

**Publisher's note:** Springer Nature remains neutral with regard to jurisdictional claims in published maps and institutional affiliations.

## METHODS

**Linear least-squares fits of mantle source Xe using Archaean atmosphere.**

Mantle source  $^{130,131,132,134,136}\text{Xe}$  compositions are modelled as four-component mixtures of initial mantle Xe, recycled atmospheric Xe, Pu-fission Xe and U-fission Xe using the method outlined in ref. <sup>16</sup>. We test two end-member scenarios: the regassed atmospheric Xe is either entirely modern or entirely ancient in its isotopic composition. We estimate the  $^{130,131,132,134,136}\text{Xe}$  isotopic composition of Archaean atmosphere based on constraints from fluid inclusions in ancient rocks<sup>2</sup>. We take the present-day atmospheric Xe composition and apply Rayleigh mass-dependent fractionation of 20‰ per atomic mass unit (AMU). The resulting composition is consistent with the atmospheric composition determined for Barberton samples after correction for fission production after closure of the fluid inclusions<sup>2</sup>. The 20‰ AMU<sup>-1</sup> fractionated model Archaean atmospheric Xe composition used for comparing the goodness of fit for the convecting mantle source composition is given in Extended Data Fig. 2e.

A sum of squared residuals of zero indicates that the mantle source composition can be fitted perfectly by mixing the four end-member components. Sums of squared residuals greater than zero indicate the sigma-normalized error in the best fit to the mantle source composition. If modern atmospheric Xe is taken as the recycled atmospheric Xe component, sums of squared residuals are zero or near-zero. If 20‰ AMU<sup>-1</sup> mass-fractionated ancient atmosphere is the recycled component, then the sums of squared residuals are much higher than zero, indicating that mantle source compositions cannot be explained by recycling of only ancient atmospheric Xe (Extended Data Fig. 2).

**Model initialization.** The concentration and isotopic composition of Xe in the mantle is tracked over time in a numerical forward model of mantle degassing, regassing and fissionogenic production. The initial concentration of  $^{130}\text{Xe}$  represents the primordial Xe component delivered and retained throughout accretion. Initial mantle  $^{130}\text{Xe}$  concentrations corresponding to Xe contributions from carbonaceous chondrites in a late veneer of 0.1%, 0.5% and 1% of the Earth's mass are tested. Figures 3, 4 correspond to model runs with a late veneer equivalent to 1% of the Earth's mass with a carbonaceous chondrite  $^{130}\text{Xe}$  concentration (based on the average of Murchison and Orgueil<sup>21</sup>). The initial mantle Xe isotopic composition is taken to be that of average carbonaceous chondrite<sup>18,22</sup>. Results for a late veneer corresponding to 0.1% and 0.5% of the Earth's mass are illustrated in Extended Data Figs. 6, 7. The initial atmospheric Xe isotopic composition is mass-fractionated with respect to modern atmosphere by 39‰ AMU<sup>-1</sup>.

**Xe concentrations in downwellings over time.** We use a Monte Carlo method to explore two functional forms for the concentration of  $^{130}\text{Xe}$  in downwelling material over time. The first is a sigmoidal function based on the generalized logistic function:

$$^{130}\text{Xe}_d(t) = \frac{^{130}\text{Xe}_d^k}{1 + e^{-\alpha(t-\beta)}} \quad (1)$$

where  $^{130}\text{Xe}_d^k$  is the carrying-capacity  $^{130}\text{Xe}$  concentration in downwellings,  $\alpha$  is the growth rate and  $\beta$  is the sigmoid inflection point. Figure 2 illustrates an example array of sigmoidal  $^{130}\text{Xe}_d$  functions tested with the model. Each sigmoid is sampled over a limited time interval and thus yields only a portion of the sigmoid shape. Therefore, the initial  $^{130}\text{Xe}_d$  values may be greater than 0 and the present-day  $^{130}\text{Xe}_d$  values are lower than or equal to the carrying capacity,  $^{130}\text{Xe}_d^k$ .

The second functional form is an exponential form:

$$^{130}\text{Xe}_d(t) = ^{130}\text{Xe}_d^{\text{final}} e^{\tau(t-T)} \quad (2)$$

where  $T$  is the age of the Earth (4.568 Gyr) and the two free parameters are  $^{130}\text{Xe}_d^{\text{final}}$  and a time constant,  $\tau$ . Time constant values between  $10^{-11}$  Gyr<sup>-1</sup> and  $5 \times 10^{-8}$  Gyr<sup>-1</sup> are explored. Extended Data Fig. 3 illustrates a coarse array of exponential  $^{130}\text{Xe}_d$  functions tested with the model. For both functional forms, we use a Monte Carlo numerical method to achieve good coverage of the free parameter space.

The present-day  $^{130}\text{Xe}_d$  concentrations tested range from zero to  $5 \times 10^8$  atoms per gram. We reiterate that regassing refers to the influx of volatiles that are transported beyond depths of magma generation and mixed into the convecting mantle. We place a broad upper limit on the present-day amount of  $^{130}\text{Xe}$  in downwelling material to constrain the collection of  $^{130}\text{Xe}_d$  time series tested with our model. Using  $^{130}\text{Xe}$  concentration data from serpentinite, altered oceanic crust and sediments<sup>5,24,25,27,31-35</sup>, we compute an upper limit on present-day regassing of Xe from constraints on regassing of water beyond depths of magma generation. We assume that serpentinite has 13 wt% H<sub>2</sub>O, altered oceanic crust has 1.2 wt% H<sub>2</sub>O<sup>36</sup> and average subducting sediment has 7.3 wt% H<sub>2</sub>O<sup>37</sup>. On the basis of mantle outgassing estimates and sea level constraints, ref. <sup>10</sup> determined an upper-limit H<sub>2</sub>O flux of  $7.0 \times 10^{14}$  g yr<sup>-1</sup> beyond depths of magma generation, corresponding to a sea level decrease of 360 m over the Phanerozoic. If this full upper limit is carried in

sediments with 7.3 wt% H<sub>2</sub>O, then this flux corresponds to  $9.6 \times 10^{15}$  g yr<sup>-1</sup> of sediment. Using the maximum sedimentary  $^{130}\text{Xe}$  concentration of  $3.2 \times 10^{10}$  atoms per gram, we compute an upper-limit present-day  $^{130}\text{Xe}$  flux beyond depths of magma generation of  $3.0 \times 10^{26}$  atoms  $^{130}\text{Xe}$  per year. This flux is then distributed over the present-day mass of downwelling per year ( $6.1 \times 10^{17}$  g yr<sup>-1</sup>) to yield a maximum present-day bulk downwelling  $^{130}\text{Xe}$  concentration of  $5.0 \times 10^8$  atoms per gram. Because the maximum present-day  $^{130}\text{Xe}_d$  in successful model realizations is much lower ( $<4 \times 10^7$  atoms per gram for sigmoidal  $^{130}\text{Xe}_d$  and  $<2 \times 10^8$  atoms per gram for exponential  $^{130}\text{Xe}_d$ ), we note that this estimated upper limit only helps to define our  $^{130}\text{Xe}_d$  parameter search windows.

**Time evolution.** Degassing occurs during partial melting of upwelling convecting mantle, and regassing occurs via the corresponding downwellings (presently at mid-ocean ridges and subduction zones, respectively). We test an exponentially decreasing mantle processing rate. The mantle processing rate is tied to the present-day ridge processing rate,  $Q_p$  ( $6.1 \times 10^{17}$  g yr<sup>-1</sup>, assuming 10% partial melting to produce  $21 \text{ km}^3 \text{ yr}^{-1}$  of crust at mid-ocean ridges, with a crustal density of  $2,900 \text{ kg m}^{-3}$ )<sup>38</sup>:

$$Q(t) = Q_p e^{\eta(T-t)} \quad (3)$$

where  $T = 4.568$  Gyr. To test different mantle processing histories with our model, we test discrete values of  $\eta$  corresponding to whole numbers of mantle reservoir masses processed over Earth history (for example,  $\eta = 8.1 \times 10^{-10}$  corresponds to  $N_{\text{res}} = 8$  with  $M_{\text{res}} = 90\%$ ). We test values from  $\eta = 1.6 \times 10^{-10}$  to  $\eta = 9.9 \times 10^{-10}$  (2–15 mantle reservoir masses ranging from 50% to 90% of the whole mantle). A linearly decreasing mantle processing rate yields similar final results. Thus, our broad conclusions are not sensitive to the functional form of the mantle processing-rate history.

For each time step, the mass of mantle ( $dM$ ) processed between time  $t_{\text{last}}$  and  $t_{\text{now}}$  is given by:

$$dM = \left( \frac{Q_p}{\eta} \right) (e^{\eta(T-t_{\text{last}})} - e^{\eta(T-t_{\text{now}})}) \quad (4)$$

The normalized mass processed per time step is  $dM/M_{\text{res}}$ , where  $M_{\text{res}}$  is the mass of the convecting mantle. Results shown in the main-text figures are obtained by taking  $M_{\text{res}}$  to be 90% of the mass of the mantle, or  $3.6 \times 10^{27}$  g. Sensitivity to the mass of the convecting mantle is shown in Extended Data Figs. 5–7.

Over a given time step, the net change in mantle  $^{130}\text{Xe}$  concentration corresponds to the balance between the  $^{130}\text{Xe}$  lost by degassing of  $dM$  by partial melting and the  $^{130}\text{Xe}$  gained by regassing via a corresponding mass of downwelling mantle with Xe concentration  $^{130}\text{Xe}_d$  (Fig. 1, Extended Data Fig. 8). The concentration of  $^{130}\text{Xe}$  in the mantle thus evolves according to:

$$^{130}\text{Xe}_{\text{now}}^m = ^{130}\text{Xe}_{\text{last}}^m + \left( \frac{dM}{M_{\text{res}}} \right) ( ^{130}\text{Xe}_{\text{last}}^d - ^{130}\text{Xe}_{\text{last}}^m ) \quad (5)$$

where the superscript m denotes the concentration in the convecting mantle and the superscript d denotes the concentration in the downwelling material (Figs. 1, 2). The mantle  $^{128}\text{Xe}$  concentration evolves similarly and is coupled to  $^{130}\text{Xe}$  via the instantaneous  $^{128}\text{Xe}/^{130}\text{Xe}$  ratios of the mantle and atmosphere (Extended Data Fig. 1):

$$^{128}\text{Xe}_{\text{now}}^m = ^{128}\text{Xe}_{\text{last}}^m + \left( \frac{dM}{M_{\text{res}}} \right) \left( ^{130}\text{Xe}_{\text{last}}^d \left( \frac{^{128}\text{Xe}}{^{130}\text{Xe}} \right)_{\text{last}}^{\text{atm}} - ^{128}\text{Xe}_{\text{last}}^m \right) \quad (6)$$

Expressions for  $^{131,132,134,136}\text{Xe}$  must additionally account for in situ production by spontaneous fission of  $^{244}\text{Pu}$  and  $^{238}\text{U}$  in the mantle. Bulk upper-mantle abundances of incompatible lithophile elements changed over Earth history in association with the growth of the continental crust. To model the depletion of the convecting mantle over time (extraction via partial melting, offset by recycling via downwellings), net U and Pu loss from the mantle at each time step tracks continental crustal growth over time (Extended Data Fig. 3).

We use three continental crust growth models (CCs) to test a range of growth rates similar to those proposed in the literature<sup>39–41</sup> (Extended Data Fig. 3). Two sigmoidal growth curves are adopted: one with relatively rapid growth (CC = 1) and one with more protracted crustal growth (CC = 2). The third growth model (CC = 3) builds the continental crust at a constant rate (linear growth), beginning 300 Myr after the formation of the Solar System. We assume that the extraction of U and Pu is directly proportional to the extraction of continental crust from the convecting mantle reservoir over time. For each combination of  $M_{\text{res}}$  and CC, we solve for the unique scaling factor  $X$  that yields a present-day U concentration<sup>42</sup> of 1.3 p.p.m. in the continental crust reservoir (mass of  $2.2 \times 10^{25}$  g)<sup>40,42</sup>, given a total

bulk (depleted convecting mantle plus continental crust) U concentration equal to the bulk silicate Earth value of 21 p.p.b.  $U^{43,44}$ . We assume that Pu and U are not fractionated from one another by crustal extraction; thus, Pu extraction tracks U extraction using the atomic ratio of the two radioactive species at any given time. On the basis of the continental crust model, which gives the mass of the continental crust over time (normalized to 1 at the present; Extended Data Fig. 3), we derive the expression for the reduction in  $^{238}U$  concentration in the convecting mantle over a given time step:

$$dCC = CC_{\text{now}} - CC_{\text{last}} \quad (7)$$

$$dU_{CC} = X \times dCC \quad (8)$$

where  $X$  is the scaling factor for  $^{238}U$  extraction for a given  $M_{\text{res}}$  and  $CC$ . The expressions for the concentration of U and Pu in the convecting mantle then reflect decay and the decrease in the  $^{238}U$  concentration over a given time step due to crustal extraction,  $dU_{CC}$  (in atoms per gram):

$$dt = t_{\text{now}} - t_{\text{last}} \quad (9)$$

$$^{238}U_{\text{now}} = ^{238}U_{\text{last}} e^{-\lambda_{238} dt} - dU_{CC} \quad (10)$$

$$^{244}Pu_{\text{now}} = ^{244}Pu_{\text{last}} e^{-\lambda_{244} dt} - \left( \frac{^{244}Pu}{^{238}U} \right)_{\text{last}} dU_{CC} \quad (11)$$

where  $\lambda_{244} = 8.6643 \times 10^{-9} \text{ yr}^{-1}$  and  $\lambda_{238} = 1.5514 \times 10^{-10} \text{ yr}^{-1}$ . The model is very weakly sensitive to the continental crust growth model (Extended Data Fig. 7).

The time evolution of a fissionogenic xenon isotope  $\psi\text{Xe}$  can thus be broken down into four equations, reflecting the primordial mantle (p.m.) budget, regassed mantle (r.m.) budget, Pu-fissionogenic budget and U-fissionogenic budget, respectively:

$$\psi\text{Xe}_{\text{now}}^{\text{p.m.}} = \psi\text{Xe}_{\text{last}}^{\text{p.m.}} \left( 1 - \frac{dM}{M_{\text{res}}} \right) \quad (12)$$

$$\psi\text{Xe}_{\text{now}}^{\text{r.m.}} = \psi\text{Xe}_{\text{last}}^{\text{r.m.}} + \left( \frac{dM}{M_{\text{res}}} \right) \left[ \left( ^{130}\text{Xe}_{\text{last}}^{\text{d}} \left( \frac{\psi\text{Xe}}{^{130}\text{Xe}} \right)_{\text{last}}^{\text{atm}} \right) - \psi\text{Xe}_{\text{last}}^{\text{r.m.}} \right] \quad (13)$$

$$\psi\text{Xe}_{\text{now}}^{\text{Pu}} = \left[ \psi\text{Xe}_{\text{last}}^{\text{Pu}} + ^{244}\text{Pu}_{\text{last}} (1 - e^{-\lambda_{244} dt}) Y_{\psi}^{\text{Pu}} \right] \left( 1 - \frac{dM}{M_{\text{res}}} \right) \quad (14)$$

$$\psi\text{Xe}_{\text{now}}^{\text{U}} = \left[ \psi\text{Xe}_{\text{last}}^{\text{U}} + ^{238}\text{U}_{\text{last}} (1 - e^{-\lambda_{238} dt}) Y_{\psi}^{\text{U}} \right] \left( 1 - \frac{dM}{M_{\text{res}}} \right) \quad (15)$$

$$\psi\text{Xe}_{\text{now}}^{\text{total}} = \psi\text{Xe}_{\text{now}}^{\text{p.m.}} + \psi\text{Xe}_{\text{now}}^{\text{r.m.}} + \psi\text{Xe}_{\text{now}}^{\text{Pu}} + \psi\text{Xe}_{\text{now}}^{\text{U}} \quad (16)$$

where  $\psi = \{131, 132, 134, 136\}$ .

The fission yield of  $^{136}\text{Xe}$  from  $^{244}\text{Pu}$  ( $Y_{136}^{\text{Pu}}$ ) is taken to be  $7 \times 10^{-5}$ , and the fission yield of  $^{136}\text{Xe}$  from  $^{238}\text{U}$  ( $Y_{136}^{\text{U}}$ ) is taken to be  $3.43 \times 10^{-8}$  (ref. 45). Yields for the other fission isotopes of Xe, calculated on the basis of fissionogenic Xe spectra, are given in Extended Data Table 2. The initial  $^{244}\text{Pu}/^{238}\text{U}$  ratio is taken to be 0.0068 (ref. 46).

The diverse half-lives of tracked radioactive species ( $^{129}\text{I}$ ,  $^{244}\text{Pu}$  and  $^{238}\text{U}$ ) necessitate a tailored time step scheme: the time step must be fine enough to accurately capture the radioactive decay of short-lived  $^{244}\text{Pu}$  early in Earth history, but after  $\sim 1$  Gyr, a very fine time step is not required for accuracy and imposes a high computational cost. We carried out convergence tests to determine the optimal time resolution scheme that accurately captures the decay of  $^{244}\text{Pu}$  and  $^{238}\text{U}$  to at least three significant figures. On the basis of this analysis, the time step is 0.1 Myr from the time when accretion is completed until 200 Myr after the formation of the Solar System, 1 Myr from 4.368 Gyr ago until 3.3 Gyr ago, and 5 Myr through the rest of Earth history to the present.

**Model success criterion 1: present-day convecting mantle  $^{130}\text{Xe}$  concentration.** The present-day concentration of  $^{130}\text{Xe}$  in the convecting mantle is estimated using the  $^3\text{He}$  mantle outgassing flux, the model present-day mantle processing rate and the  $^{130}\text{Xe}/^3\text{He}$  ratio of the mid-ocean ridge basalt mantle source. Estimates of the mantle outgassing flux vary, and a range of 400–850 moles of  $^3\text{He}$  per year covers recent estimates<sup>47–49</sup>. Our model present-day mantle processing rate is based on  $21 \text{ km}^3 \text{ yr}^{-1}$  of oceanic crust production<sup>38</sup>, assuming an average crustal density of

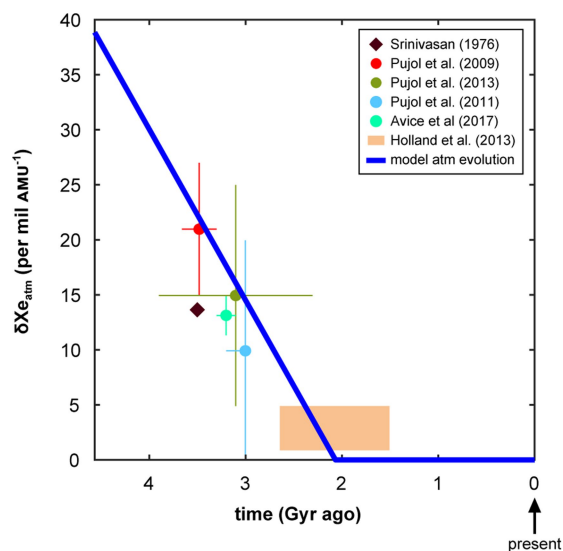
$2.9 \text{ g cm}^{-3}$  and 10% partial melting to produce oceanic crust on average<sup>50</sup>. The convecting mantle  $^{130}\text{Xe}/^3\text{He}$  ratio is estimated to be  $1.1 \times 10^{-3}$  based on a robust fit of  $^{129}\text{Xe}/^{130}\text{Xe}$  versus  $^3\text{He}/^{130}\text{Xe}$  data from the popping rock 2IID43 (ref. 51) and taking the mantle source  $^{129}\text{Xe}/^{130}\text{Xe}$  ratio<sup>12</sup> to be 7.8. Using these values, we determine a convecting mantle  $^{130}\text{Xe}$  concentration range of  $4.3 \times 10^5$  to  $9.2 \times 10^5$  atoms  $^{130}\text{Xe}$  per gram. This estimate is about two times lower than another recent estimate<sup>21</sup>. However, Marty<sup>21</sup> uses a higher ridge  $^3\text{He}$  outgassing flux of  $1,000 \pm 250$  moles per year<sup>52</sup> to constrain the absolute concentration of  $^{130}\text{Xe}$  in the upper mantle. Halliday<sup>53</sup> also provides an estimate of mantle  $^{130}\text{Xe}$  concentration, but this is an estimate of the bulk mantle based partially on data from plume-derived samples. Model realizations that produce present-day convecting mantle  $^{130}\text{Xe}$  concentrations between  $4.3 \times 10^5$  and  $9.2 \times 10^5$  atoms per gram are considered successful.

**Model success criterion 2: present-day convecting mantle Xe isotopic composition.** The primordial mantle Xe isotopic composition is taken to be chondritic<sup>22</sup>. In successful model realizations, the mantle Xe isotopic composition evolves from average carbonaceous chondrite<sup>17,18</sup> to the present-day mantle range via the addition of Xe derived from Pu fission and U fission, regassing of atmospheric Xe that evolves as a function of time (Extended Data Fig. 1) and degassing. Constraints on the convecting mantle  $^{128}\text{Xe}/^{130}\text{Xe}$  ratio are based on measurements in well gases and mantle-derived basalts.  $^{128}\text{Xe}/^{130}\text{Xe}$  ratios up to  $\sim 0.478$  are measured in well gases<sup>11</sup>. Model realizations that produce present-day mantle  $^{128}\text{Xe}/^{130}\text{Xe}$  ratios between 0.475 and 0.478 are considered successful. Constraints on the  $^{132}\text{Xe}$ -normalized Xe isotope ratios are based on measurements of mantle-derived basalts<sup>14,16</sup> and well gases<sup>11,23</sup>. Extended Data Table 2 gives the present-day range of mantle Xe isotopic compositions used to determine successful model realizations. **Code availability.** A Matlab code for modelling mantle Xe isotopic evolution is available from the authors upon reasonable request.

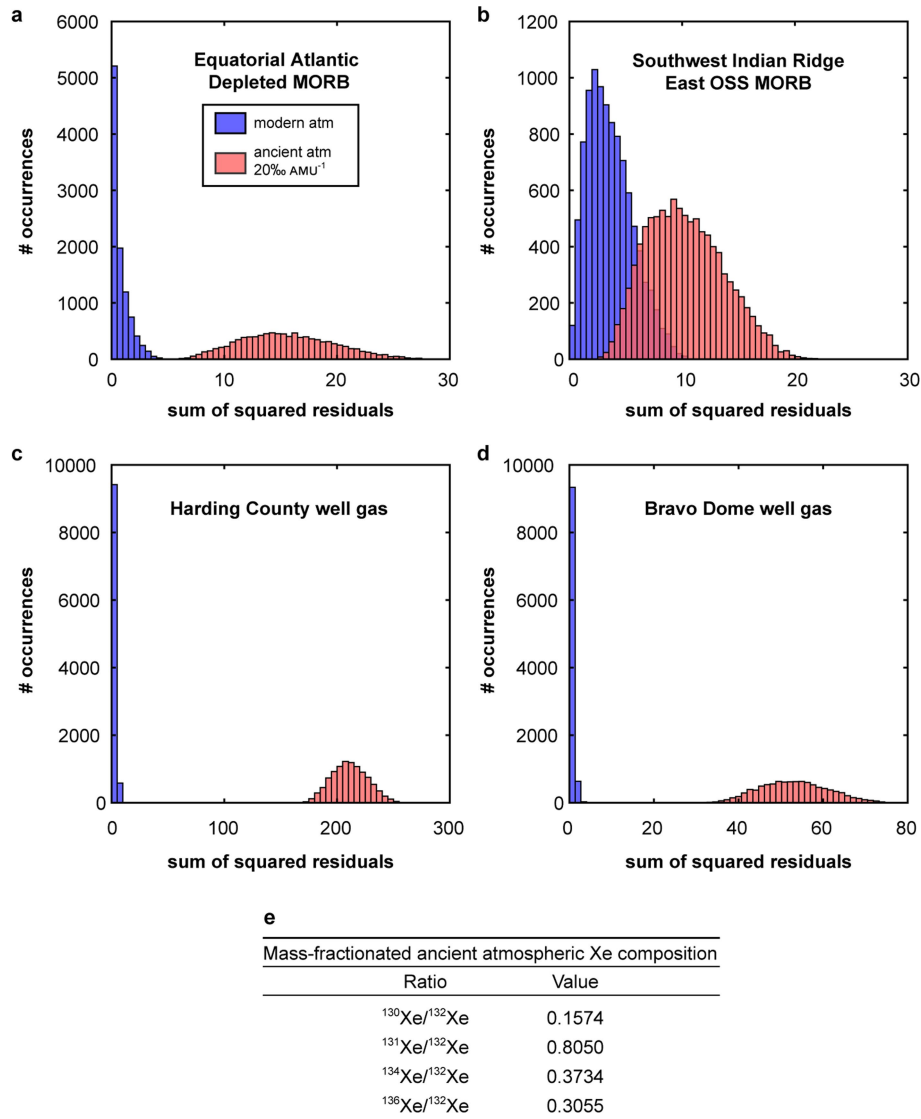
**Data availability.** The data that support the findings of this study are available from the corresponding author upon reasonable request.

- Kumagai, H., Dick, H. J. & Kaneoka, I. Noble gas signatures of abyssal gabbros and peridotites at an Indian Ocean core complex. *Geochem. Geophys. Geosyst.* **4**, 9017 (2003).
- Matsuda, J. I. & Matsubara, K. Noble gases in silica and their implication for the terrestrial “missing” Xe. *Geophys. Res. Lett.* **16**, 81–84 (1989).
- Matsuda, J.-I. & von Herzen, R. Thermal conductivity variation in a deep-sea sediment core and its relation to  $\text{H}_2\text{O}$ , Ca and Si content. *Deep-Sea Res. A* **33**, 165–175 (1986).
- Podosek, F., Honda, M. & Ozima, M. Sedimentary noble gases. *Geochim. Cosmochim. Acta* **44**, 1875–1884 (1980).
- Staudacher, T. & Allègre, C. J. Recycling of oceanic crust and sediments: the noble gas subduction barrier. *Earth Planet. Sci. Lett.* **89**, 173–183 (1988).
- Jarrard, R. D. Subduction fluxes of water, carbon dioxide, chlorine, and potassium. *Geochem. Geophys. Geosyst.* **4**, 8905 (2003).
- Plank, T. & Langmuir, C. H. The chemical composition of subducting sediment and its consequences for the crust and mantle. *Chem. Geol.* **145**, 325–394 (1998).
- Crisp, J. A. Rates of magma emplacement and volcanic output. *J. Volcanol. Geotherm. Res.* **20**, 177–211 (1984).
- Dhuime, B., Hawkesworth, C. J., Cawood, P. A. & Storey, C. D. A change in the geodynamics of continental growth 3 billion years ago. *Science* **335**, 1334–1336 (2012).
- McLennan, S. M. & Taylor, S. R. Geochemical constraints on the growth of the continental crust. *J. Geol.* **90**, 347–361 (1982).
- Pujol, M., Marty, B., Burgess, R., Turner, G. & Philippot, P. Argon isotopic composition of Archaean atmosphere probes early Earth geodynamics. *Nature* **498**, 87–90 (2013).
- Rudnick, R. & Gao, S. *Treatise on Geochemistry* Vol. 3 (eds Holland, H. D. & Turekian, K. K.) 1–64 (Elsevier, 2003).
- McDonough, W. F. & Sun, S. S. The composition of the Earth. *Chem. Geol.* **120**, 223–253 (1995).
- Palme, H. & O'Neill, H. S. C. in *Treatise on Geochemistry* Vol. 2 (eds Holland, H. D. & Turekian, K. K.) 1–38 (Elsevier, Amsterdam, 2004).
- Tolstikhin, I., Marty, B., Porcelli, D. & Hofmann, A. Evolution of volatile species in the Earth’s mantle: a view from xenology. *Geochim. Cosmochim. Acta* **136**, 229–246 (2014).
- Hudson, G. B., Kennedy, B. M., Podosek, F. A. & Hohenberg, C. M. In *Proc. 19th Lunar and Planetary Science Conference* 547–557 (Lunar and Planetary Institute, 1989).
- Bianchi, D. et al. Low helium flux from the mantle inferred from simulations of oceanic helium isotope data. *Earth Planet. Sci. Lett.* **297**, 379–386 (2010).
- Holzer, M. et al. Objective estimates of mantle  $^3\text{He}$  in the ocean and implications for constraining the deep ocean circulation. *Earth Planet. Sci. Lett.* **458**, 305–314 (2017).
- Schlitzer, R. Quantifying He fluxes from the mantle using multi-tracer data assimilation. *Phil. Trans. R. Soc. A* **374**, 20150288 (2016).
- Klein, E. M. & Langmuir, C. H. Global correlations of ocean ridge basalt chemistry with axial depth and crustal thickness. *J. Geophys. Res.* **92**, 8089–8115 (1987).

51. Moreira, M., Kunz, J. & Allegre, C. Rare gas systematics in Popping Rock: isotopic and elemental compositions in the upper mantle. *Science* **279**, 1178–1181 (1998).
52. Craig, H., Clarke, W. & Beg, M. Excess  $^3\text{He}$  in deep water on the East Pacific Rise. *Earth Planet. Sci. Lett.* **26**, 125–132 (1975).
53. Halliday, A. N. The origins of volatiles in the terrestrial planets. *Geochim. Cosmochim. Acta* **105**, 146–171 (2013).
54. Holland, G. et al. Deep fracture fluids isolated in the crust since the Precambrian era. *Nature* **497**, 357–360 (2013).
55. Srinivasan, B. Barites: anomalous xenon from spallation and neutron-induced reactions. *Earth Planet. Sci. Lett.* **31**, 129–141 (1976).
56. Alexander, E. C. Jr, Lewis, R. S., Reynolds, J. H. & Michel, M. C. Plutonium-244: confirmation as an extinct radioactivity. *Science* **172**, 837–840 (1971).
57. Lewis, R. S. Rare-gases in separated whitlockite from St. Severin chondrites: xenon and krypton from fission extinct Pu-244. *Geochim. Cosmochim. Acta* **39**, 417–432 (1975).
58. Wetherill, G. W. Spontaneous fission yields from uranium and thorium. *Phys. Rev.* **92**, 907–912 (1953).
59. Hebeda, E. H., Schultz, L. & Freundel, M. Radiogenic, fissionogenic and nucleogenic noble gases in zircons. *Earth Planet. Sci. Lett.* **85**, 79–90 (1987).
60. Eikenberg, J., Signer, P. & Wieler, R. U-Xe, U-Kr, AND U-Pb systematics for dating uranium minerals and investigations of the production of nucleogenic neon and argon. *Geochim. Cosmochim. Acta* **57**, 1053–1069 (1993).
61. Ragettli, R. A., Hebeda, E. H., Signer, P. & Wieler, R. Uranium xenon chronology: precise determination of  $\lambda_{\text{sf}}^{136}\text{Y}_{\text{sf}}$  for spontaneous fission of  $^{238}\text{U}$ . *Earth Planet. Sci. Lett.* **128**, 653–670 (1994).



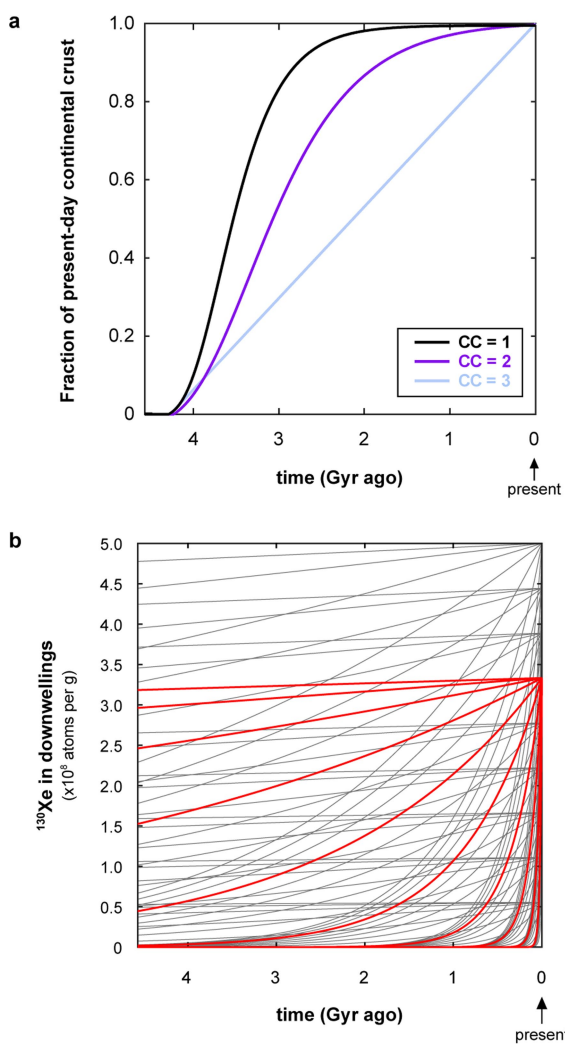
**Extended Data Fig. 1 | Atmospheric Xe mass fractionation relative to the modern composition over time.** Figure adapted from ref. <sup>2</sup>. Xe measured in Archaean barites, fluid inclusions in quartz from Archaean cherts and deep crustal fluids of various age are shown with associated  $2\sigma$  uncertainties<sup>1,2,20,41,54,55</sup>. The blue line shows the model atmospheric Xe mass fractionation over time. We assume that the initial Xe isotopic composition of the atmosphere is Rayleigh-mass-fractionated by  $\sim 39\text{‰ AMU}^{-1}$  relative to the modern atmosphere and that the degree of mass fractionation decreases linearly until 2 Gyr ago (Ga), when the atmosphere reaches its present composition.



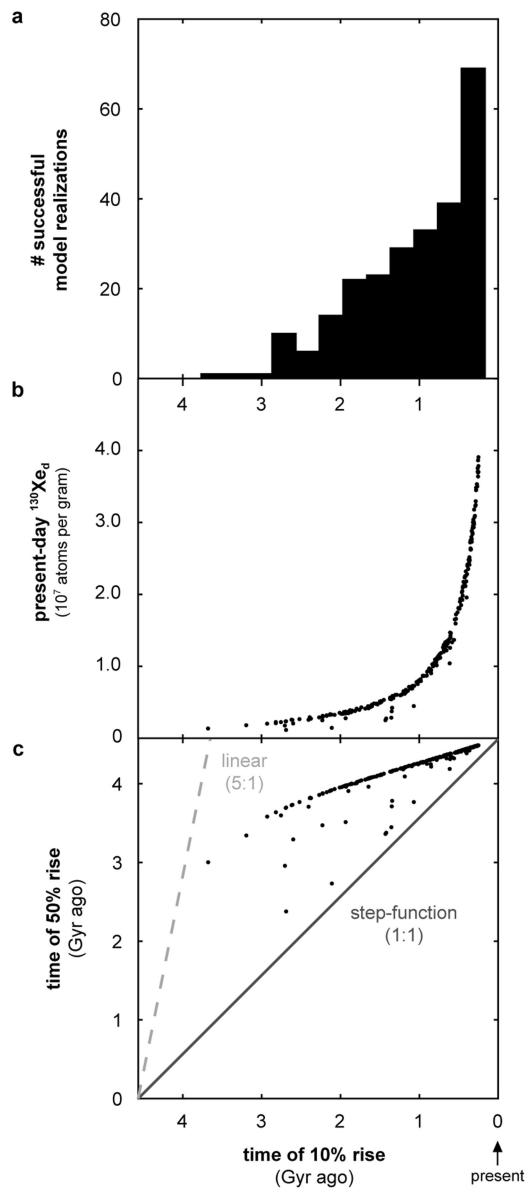
**Extended Data Fig. 2 | Sum of squared residuals from least-squares fitting of mantle source compositions using either modern or ancient atmospheric Xe.** Mantle source  $^{130,131,132,134,136}\text{Xe}$  compositions are modelled as four-component mixtures of initial mantle Xe, recycled atmospheric Xe, and Xe from the fission of Pu and U. A sum of squared residuals of zero indicates that the mantle source composition can be fitted perfectly by mixing the four end-member components. Sums of squared residuals greater than zero indicate the sigma-normalized error in the best fit compared to the mantle source composition. Using modern atmospheric Xe as the regassed atmospheric Xe component, sums of squared residuals are zero or near-zero. Using ancient atmosphere, sums of squared residuals are much higher than zero, indicating that mantle

source compositions cannot be explained by regassing of only ancient atmospheric Xe. The ancient atmospheric Xe composition used here corresponds to 20‰  $\text{AMU}^{-1}$  Rayleigh fractionation applied to the modern atmospheric composition and agrees with fission-corrected ancient atmosphere derived from fluid inclusions in Archaean rocks<sup>2</sup>.

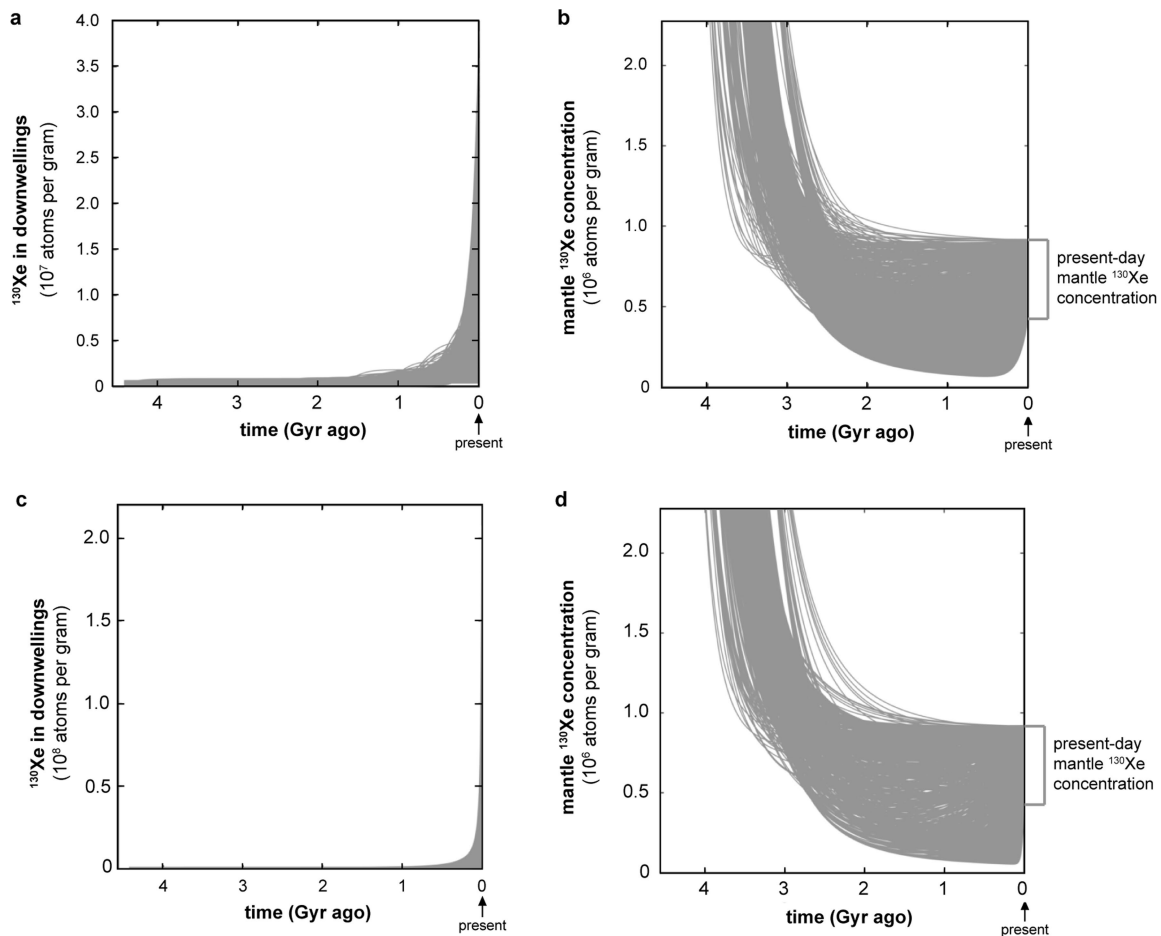
**a–e**, Mantle source compositions for Equatorial Atlantic depleted mid-ocean ridge basalt (MORB)<sup>14</sup> (**a**), Southwest Indian Ridge Eastern Orthogonal Supersegment MORB<sup>16</sup> (**b**), Harding County well gas<sup>23</sup> (**c**) and Bravo Dome well gas<sup>11</sup> (**d**) are fitted using the Monte Carlo method ( $n = 10,000$ ) described in ref. <sup>16</sup>, with average carbonaceous chondrite as the initial mantle composition<sup>22</sup>, and either modern or 20‰  $\text{AMU}^{-1}$  fractionated atmosphere (**e**) as the recycled component.



**Extended Data Fig. 3 | Continental crust growth models and exponential  $^{130}\text{Xe}_d$  time series examples.** **a**,  $^{238}\text{U}$  (and a small amount of  $^{244}\text{Pu}$ ) extraction from the mantle by partial melting is offset by recycling of sediments at subduction zones at each time step. We model net extraction of U and any extant Pu from the mantle as directly tracking continental crust growth over time (Methods). Three CCs are adopted: two sigmoidal curves that approximate literature continental crust growth curves ('CC = 1' and 'CC = 2') and one linear growth curve ('CC = 3')<sup>39–41</sup>. **b**, Example of exponential  $^{130}\text{Xe}_d$  time series tested with our forward model of mantle Xe evolution. Two parameters describe the exponential function (Methods):  $^{130}\text{Xe}_d^{\text{final}}$ , the final  $^{130}\text{Xe}$  concentration in downwellings, and  $\tau$ , the exponential time constant. Grey lines represent a collection of exponentials with discrete variation in  $^{130}\text{Xe}_d^{\text{final}}$  and  $\tau$ . A subset with a constant  $^{130}\text{Xe}_d^{\text{final}}$  and varying  $\tau$  is highlighted in red. The time constant  $\tau$  is varied from  $10^{-11} \text{ Gyr}^{-1}$  to  $5 \times 10^{-8} \text{ Gyr}^{-1}$ , with small  $\tau$  corresponding to slow growth. Examples for nine different  $^{130}\text{Xe}_d^{\text{final}}$  values are shown, with an upper bound of  $5 \times 10^8$  atoms  $^{130}\text{Xe}$  per gram (Methods).

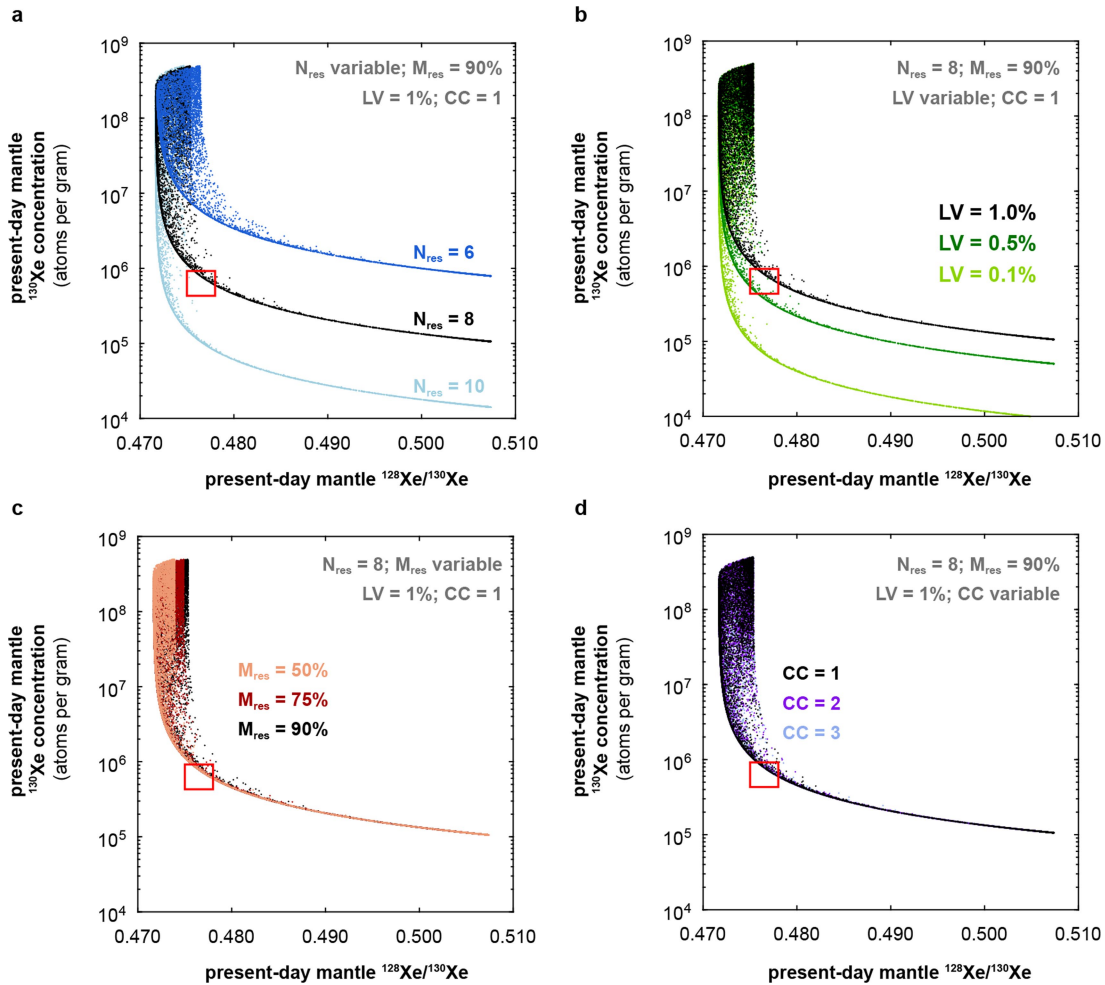


**Extended Data Fig. 4 | Characterization of successful regassing histories.** Diverse regassing history shapes are generated by sampling a limited time interval for a variety of growth rates and inflection times (Fig. 2). To provide a common point of comparison for the evolving conditions within downwellings, we sort results by the time when  $^{130}\text{Xe}_d$  has increased by 10% between its initial and final values (time of 10% rise). **a**, Times of 10% rise for successful regassing histories. Most successful model realizations have a time of 10% rise later than 2.5 Gyr ago. **b**, Model realizations with high present-day  $^{130}\text{Xe}_d$  values are uniformly characterized by late 10% rise times, indicating that in these model realizations downwelling Xe concentrations remain very low throughout most of Earth history. **c**, Variation in sigmoidal growth rates (parameter  $\alpha$ ) allows testing of near-linear (low  $\alpha$ , sampling for a limited time interval) or near-step (high  $\alpha$ ) functions. Near-linear model realizations have a time of 50% rise that is about five times the time of 10% rise (dashed light-grey line), whereas step functions approach a 1:1 line (solid dark-grey line). Successful regassing histories with late times of 10% rise are characterized by rapid growth, approaching a step function, to a relatively high present-day  $^{130}\text{Xe}_d$ .



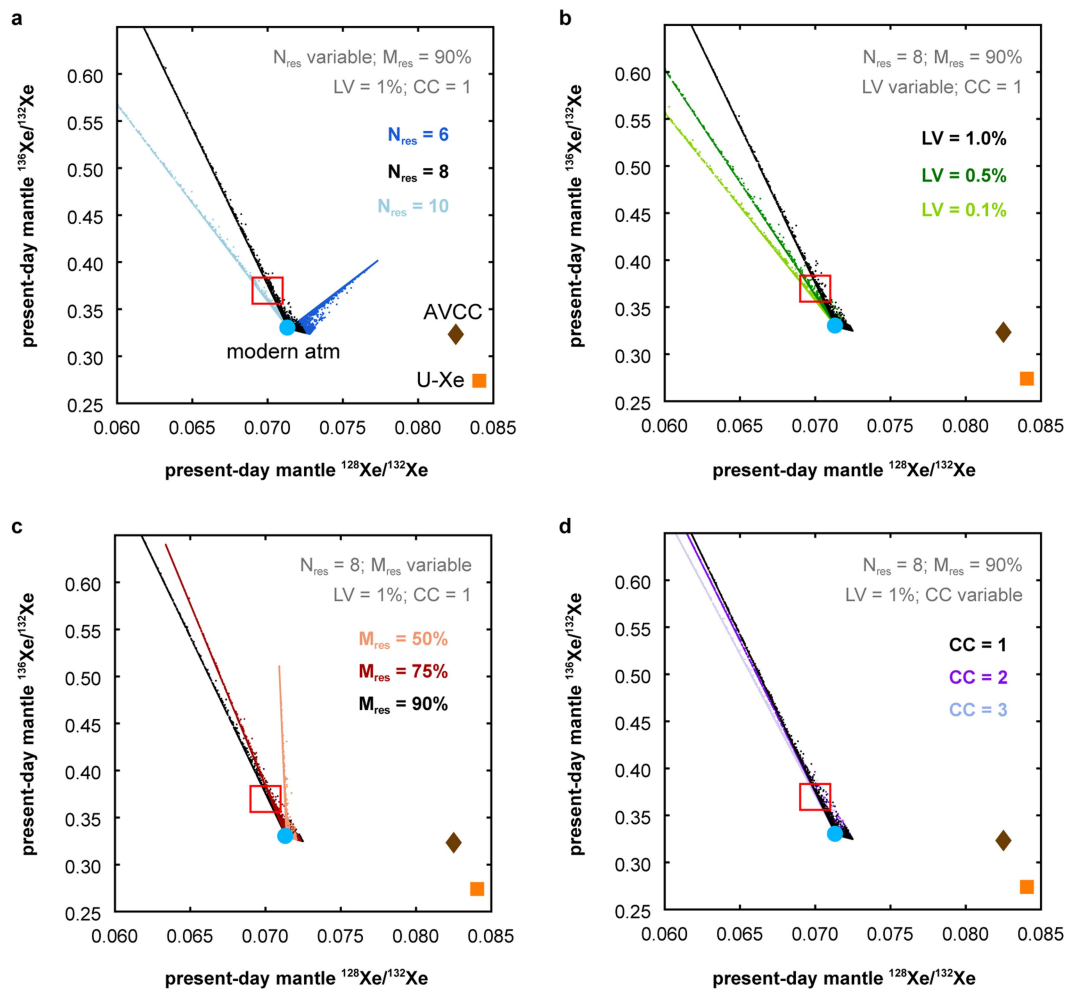
**Extended Data Fig. 5 | Successful regassing histories for varying model parameters.** **a–d**, To test model sensitivity to the input parameters, we vary the number of mantle reservoir masses processed ( $N_{\text{res}}$ ), convecting mantle reservoir mass ( $M_{\text{res}}$ ), initial  $^{130}\text{Xe}$  concentration (LV) and continental crust model (CC), and collect all successful  $^{130}\text{Xe}_d$  (**a**, **c**) and mantle  $^{130}\text{Xe}$  concentrations (**b**, **d**) over time. For sigmoidal  $^{130}\text{Xe}_d$ , solutions are found for  $N_{\text{res}} = \{5, 6, 7, 8, 9\}$ ,  $M_{\text{res}}$  of 50%, 75% and 90% of the whole mantle mass, LV of 0.1%, 0.5% and 1% chondritic late veneers, and all three CCs. Extended Data Figs. 6, 7 illustrate trade-offs between

individual parameters; for instance, high  $N_{\text{res}}$  values generate solutions only with high LV. For all sigmoidal solutions, regassing is limited early in Earth history, and the mantle shifts from net degassing to net regassing after  $\sim 2.5$  Gyr ago. For exponential  $^{130}\text{Xe}_d$ , solutions are found for  $N_{\text{res}} = \{5, 6, 7, 8, 9\}$ ,  $M_{\text{res}}$  of 50%, 75% and 90% of the whole mantle mass, LV of 0.1%, 0.5% and 1% chondritic late veneers, and all three CCs. For all solutions, regassing is limited early in Earth history, and the mantle shifts from net degassing to net regassing after  $\sim 2.5$  Gyr ago.



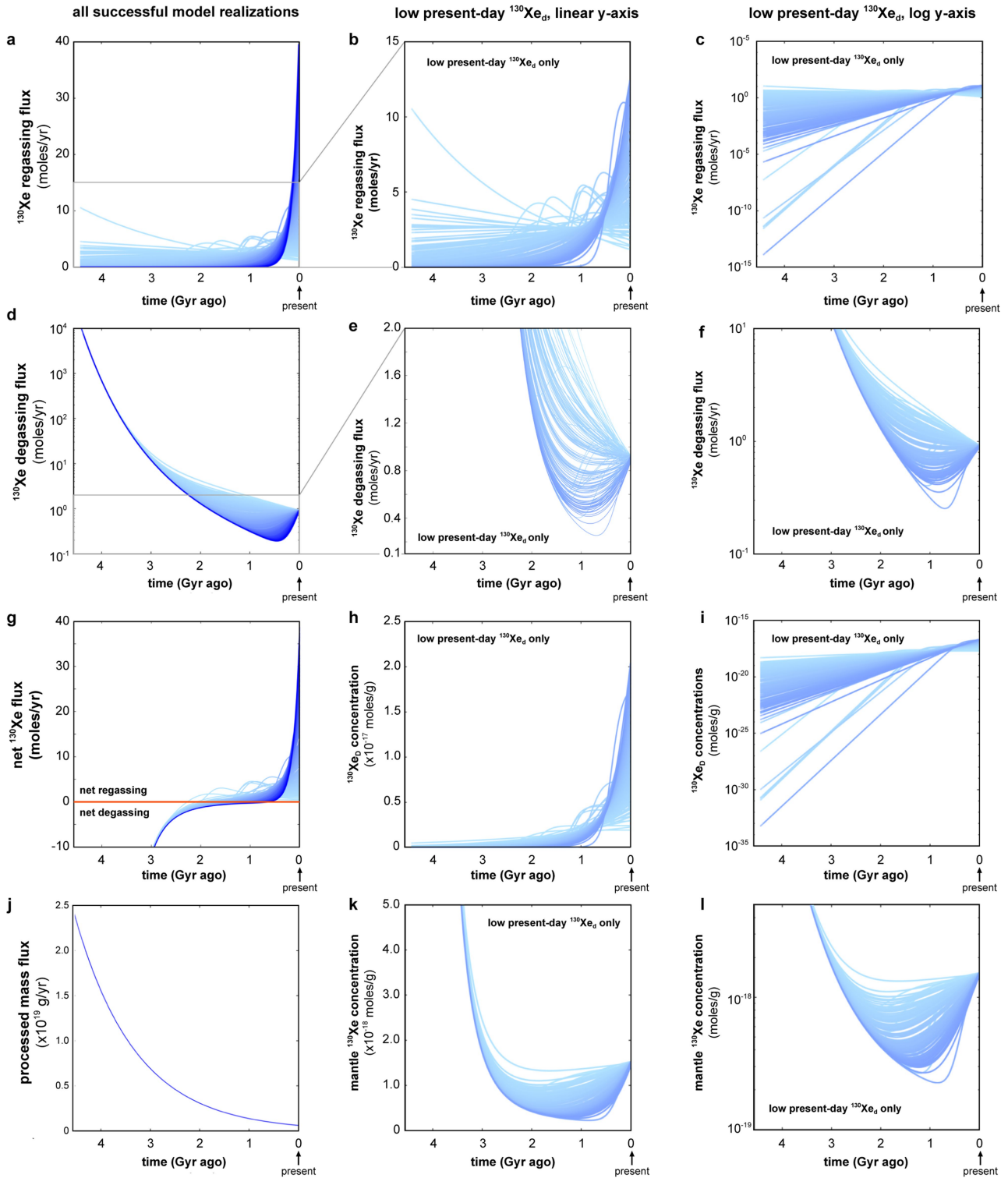
**Extended Data Fig. 6 | Sensitivity of  $^{130}\text{Xe}$  and  $^{128}\text{Xe}/^{130}\text{Xe}$  to model parameters.** Present-day mantle  $^{130}\text{Xe}$  concentration and the ratio of two primordial stable isotopes,  $^{128}\text{Xe}$  and  $^{130}\text{Xe}$  are shown for different model parameter combinations. Four parameters are explored: those affecting the mantle processing-rate history ( $M_{\text{res}}$  and  $N_{\text{res}}$ ), LV (initial  $^{130}\text{Xe}$  concentrations corresponding to a late veneer fraction between 0.1% and 1%) and CC (Extended Data Fig. 3). In each panel, three of these parameters are held constant and the other is varied to illustrate model sensitivity to the varied parameter. Each cloud of points represents the range of present-day  $^{130}\text{Xe}$  and  $^{128}\text{Xe}/^{130}\text{Xe}$  generated by different degassing histories for the specified  $N_{\text{res}}$ ,  $M_{\text{res}}$ , LV and CC. The red rectangle indicates the estimated present-day mantle  $^{130}\text{Xe}$  concentration and  $^{128}\text{Xe}/^{130}\text{Xe}$  range. Dots that fall within the red rectangle represent the family of degassing histories that successfully reproduce the present-day mantle composition for each parameter combination. The reference case shown in Figs. 3, 4 ( $M_{\text{res}} = 90\%$ ,  $N_{\text{res}} = 8$ , LV = 1%, CC = 1) is shown as

a cloud of black points in all panels. **a**, A higher mantle processing rate ( $N_{\text{res}} = 10$ ) results in low  $^{130}\text{Xe}$  concentrations for successful  $^{128}\text{Xe}/^{130}\text{Xe}$  ratios, and  $^{128}\text{Xe}/^{130}\text{Xe}$  ratios that are too low for successful  $^{130}\text{Xe}$  concentrations. **b**, Higher late-veener fractions correspond to higher initial  $^{130}\text{Xe}$  concentrations in the mantle. For the same mantle processing-rate history, LV = 0.1% yields present-day mantle  $^{130}\text{Xe}$  concentrations that are too low given successful  $^{128}\text{Xe}/^{130}\text{Xe}$  ratios. The effect of low LV can be offset by lowering  $N_{\text{res}}$  and thus decreasing the total amount of degassing over Earth history; thus,  $N_{\text{res}}$  and LV can be co-varied to find solutions. **c**, The effect of  $M_{\text{res}}$  is minimal because degassing is parameterized through the number of reservoir masses processed over Earth history. Some difference is evident at high present-day mantle  $^{130}\text{Xe}$  abundances because the same  $^{130}\text{Xe}_d$  degassing rate parameter space is explored against different absolute degassing rates. **d**, The continental crust model has no effect on budgets of primordial Xe isotopes.



**Extended Data Fig. 7 | Sensitivity of fissiogenic Xe to model parameters.** Present-day outcomes are shown in  $^{128}\text{Xe}$ – $^{132}\text{Xe}$ – $^{136}\text{Xe}$  isotopic space for different model parameter combinations. Four parameters are explored: parameters affecting the mantle processing-rate history ( $M_{\text{res}}$  and  $N_{\text{res}}$ ), the initial mantle  $^{130}\text{Xe}$  concentration ( $LV = 0.1\%$ – $1\%$ ), and  $CC$  (Extended Data Fig. 3). In each panel, three of these parameters are held constant and the other is varied to illustrate model sensitivity to the varied parameter. Each cloud of points represents the range of present-day  $^{128}\text{Xe}/^{132}\text{Xe}$  and  $^{136}\text{Xe}/^{132}\text{Xe}$  generated by different regassing histories given the specified  $N_{\text{res}}$ ,  $M_{\text{res}}$ ,  $LV$  and  $CC$ . The red rectangle indicates the estimated present-day mantle  $^{128}\text{Xe}/^{132}\text{Xe}$  and  $^{136}\text{Xe}/^{132}\text{Xe}$  range. Dots that fall within the red rectangle represent the family of regassing histories that successfully reproduce present-day

mantle composition for each parameter combination. The reference case shown in the main-text figures ( $M_{\text{res}} = 90\%$ ,  $N_{\text{res}} = 8$ ,  $LV = 1\%$ ,  $CC = 1$ ) is shown as a cloud of black points in all panels. The orange square is U-Xe, the brown diamond is average carbonaceous chondrites (AVCC) and the blue circle is the modern atmosphere. **a**, Higher mantle processing rates push present-day compositions towards fissiogenic Xe components. **b**, Lower late-veener fractions correspond to present-day compositions closer to fissiogenic Xe components. **c**, A relatively low mass of the convecting mantle means that the mantle must be more depleted in U to satisfy mass balance with the continental crust (Methods). Thus, for low  $M_{\text{res}}$ , the impact of fission is muted compared to high  $M_{\text{res}}$ . **d**, The continental crust model has a limited effect on present-day Xe isotopic compositions.



Extended Data Fig. 8 | See next page for caption.

**Extended Data Fig. 8 |  $^{130}\text{Xe}$  fluxes over time in successful model realizations.** **a–l**, Regassing fluxes (**a–c**), degassing fluxes (**d–f**), net fluxes (**g**),  $^{130}\text{Xe}_d$  concentrations (**h, i**), mass flux (**j**) and mantle  $^{130}\text{Xe}$  concentrations (**k, l**) are illustrated for an initial mantle  $^{130}\text{Xe}$  concentration of  $3.2 \times 10^8$  atoms per gram ( $LV = 1\%$ ), a convecting mantle reservoir that is 90% of the mass of the whole mantle, and 8 mantle reservoir masses processed over Earth history. Fluxes are reported in moles per year and concentrations are reported in moles per gram. Panels in the left column show results from all successful model realizations (same results as those shown in Figs. 3, 4) and illustrate the  $^{130}\text{Xe}$  regassing flux (**a**),  $^{130}\text{Xe}$  degassing flux (**d**),  $^{130}\text{Xe}$  net flux (**g**) and mass flux over time (**j**). Panels in the central column show zoomed-in windows with only low- $^{130}\text{Xe}_d$  successful model realizations (light-blue lines), as these largely overlap with each other and are difficult to resolve in the full-scale panels. The right column replicates the central column with semi-logarithmic axes. The regassing  $^{130}\text{Xe}$  flux time series (**a–c**) is

the product of the downwelling mass flux time series (**j**; exponentially decreasing with time) and the  $^{130}\text{Xe}_d$  concentration over time (sigmoidally increasing; **h, i**). Time series for  $^{130}\text{Xe}$  regassing fluxes with high present-day  $^{130}\text{Xe}_d$  (darkest-blue lines in **a**) start near zero owing to near-zero  $^{130}\text{Xe}$  concentrations and then rapidly rise as the  $^{130}\text{Xe}_d$  concentration increases faster than the modest decline in mass flux later in Earth history.  $^{130}\text{Xe}$  flux time series with low present-day  $^{130}\text{Xe}_d$  (lightest-blue lines in **a–c**) start a protracted, low-magnitude rise relatively early in Earth history. These translate to regassing flux time series that start near zero, rise and then decline with the exponentially decreasing mass flux (**b, c**). Time series for  $^{130}\text{Xe}$  degassing fluxes (**d–f**) are the product of the downwelling mass flux time series (**j**) and the mantle  $^{130}\text{Xe}$  concentration over time (**k, l**), which responds to both degassing and regassing. The net flux over time (**g**) is the difference between the regassing flux and degassing flux at any given time. The mantle shifts from net degassing to net regassing at some time after 2.5 Gyr ago.

## Extended Data Table 1 | Notation

## Subscripts and superscripts

d	in downwellings
m	in convecting mantle (mid-ocean ridge basalt source)
p	primordial
r	regassed

## Regassing history

$^{130}\text{Xe}_d$  concentration of  $^{130}\text{Xe}$  in downwellings over time (atoms/g)

*Sigmoidal  $^{130}\text{Xe}_d$  parameters*

$^{130}\text{Xe}_d^k$	$^{130}\text{Xe}_d$ sigmoid carrying capacity (0 to $5 \times 10^8$ atoms/g)
$\alpha$	sigmoid growth rate ( $10^{-10}$ to $10^{-8}$ Gyr $^{-1}$ )
$\beta$	sigmoid inflection time (0.08 - 10 Gyr)

*Exponential  $^{130}\text{Xe}_d$  parameters*

$^{130}\text{Xe}_d^{\text{final}}$	$^{130}\text{Xe}_d$ in the present day (0 to $5 \times 10^8$ atoms/g)
$\tau$	$^{130}\text{Xe}_d$ time constant ( $10^{-11}$ to $5 \times 10^{-8}$ Gyr $^{-1}$ )

## Mantle processing and fissionogenic ingrowth

LV	late veneer fraction (0.1%, 0.5%, 1% Earth mass)
$M_{\text{res}}$	mass of convecting mantle reservoir (50%-90%, $2 \times 10^{27}$ to $3.6 \times 10^{27}$ g)
$N_{\text{res}}$	number of reservoir masses processed over Earth history
Q	mantle processing rate (g/yr)
$Q_p$	present-day mantle processing rate ( $6.1 \times 10^{17}$ g/yr)
$\eta$	processing rate time constant
T	age of the Earth (4.568 Gyr)
t	time (yr)
dM	mass of mantle processed in a time step (g)
dU <sub>CC</sub>	change in $^{238}\text{U}$ concentration in convecting mantle in a time step (atoms/g)
CC	continental crust growth model (1,2,3)
$\lambda_{244}$	$^{244}\text{Pu}$ decay constant ( $8.6643 \times 10^{-8}$ yr $^{-1}$ )
$\lambda_{238}$	$^{238}\text{U}$ decay constant ( $1.5514 \times 10^{-10}$ yr $^{-1}$ )
$Y_{\text{Pu}}^{136}$	Fission yield of $^{136}\text{Xe}$ from $^{244}\text{Pu}$ ( $7 \times 10^{-5}$ )
$Y_{\text{U}}^{136}$	Fission yield of $^{136}\text{Xe}$ from $^{238}\text{U}$ ( $3.43 \times 10^{-8}$ )
$\psi$	Fission Xe isotope mass (131, 132, 134, 136)

**Extended Data Table 2 | Xe isotopic compositions**

ratio	Present-day convecting mantle*		Fission Xe	
	mantle min	mantle max	$^{244}\text{Pu}\dagger$	$^{238}\text{U}\ddagger$
$^{128}\text{Xe}/^{130}\text{Xe}$	0.475	0.478	n/a	n/a
$^{128}\text{Xe}/^{132}\text{Xe}$	0.069	0.071	0	0
$^{130}\text{Xe}/^{132}\text{Xe}$	0.1445	0.1493	0	0
$^{131}\text{Xe}/^{132}\text{Xe}$	0.7608	0.7786	0.1449	0.2777
$^{134}\text{Xe}/^{132}\text{Xe}$	0.4082	0.4302	1.437	1.041
$^{136}\text{Xe}/^{132}\text{Xe}$	0.3559	0.3835	1.738	1.120

min, minimum; max, maximum; n/a, not applicable.

\*Limits derived from refs <sup>11,14,16,23</sup>.

†Error-weighted average of data from refs <sup>46,56,57</sup>.

‡Error-weighted average of data from refs <sup>58-61</sup>.